



Title	Fabrication and characterization of semiconducting and ferromagnetic nanostructures on crystallized Al ₂ O ₃ layers
Author(s)	崎田, 晋哉
Citation	北海道大学. 博士(工学) 甲第12186号
Issue Date	2016-03-24
DOI	10.14943/doctoral.k12186
Doc URL	http://hdl.handle.net/2115/62171
Type	theses (doctoral)
File Information	Shinya_Sakita.pdf



[Instructions for use](#)

Doctoral Dissertation

博士論文

Fabrication and characterization of semiconducting and
ferromagnetic nanostructures on crystallized Al_2O_3 layers

(結晶化 Al_2O_3 膜上の半導体及び強磁性体ナノ構造の作製と評価に関する研究)

Graduate School of Information Science and Technology,

Hokkaido University

北海道大学大学院情報科学研究科

Shinya Sakita

崎田 晋哉

A dissertation submitted in partial fulfillment
of the requirements for the degree of
Doctor of Philosophy (Engineering)
in Hokkaido University, February, 2016.

Dissertation Supervisor

Associate Professor Shinjiro Hara

Acknowledgements

This dissertation describes a part of research work carried out at Research Center for Integrated Quantum Electronics (RCIQE) and Graduate School of Information Science and Technology, Hokkaido University, under the direction of Professor Takashi Fukui, while I was graduate student at the Graduate School of Information Science Technology.

I especially wish to express my sincere appreciation to Supervisor, Associate Professor Shinjiro Hara. This work would never be accomplished without his invaluable support, guidance, and encouragement. I am greatly happy to study and research for six years under his supervision.

I would like to express my sincere thanks to Professor Tamotsu Hashizume, and Professor Junichi Motohisa for their continual support and encouragement.

I would like to express my appreciation to Professor Takashi Fukui, Professor Eiichi Sano, Professor Kanji Yoh, Professor Seiya Kasai, Associate Professor Masamichi Akazawa, Associate Professor Taketomo Sato, Associate Professor Masayuki Ikebe, and Assistant Professor Katsuhiko Tomioka for their encouragement and fruitful discussions.

I would like to express my appreciation to Professor Masafumi Yamamoto, Professor Ikuo Suemune, Professor Masato Motomura, Professor Yasuo Takahashi, Professor Akihiro Murayama, Professor Kazuhisa Sueoka, and Professor Akihisa Tomita, for their invaluable lectures and encouragement.

Acknowledgement

I would like to say thanks to the member of our research group, Dr. Takuya Sato, Mr. Nobuhiro Isomura, Dr. Keitaro Ikejiri, Mr. Tomotaka Tanaka, Mr. Shingo Ito, Mr. Dr. Masatoshi yoshimura, Mr. Shouta Fujisawa, Mr. Kohei Morita, Mr. Keita Komagata, Mr. Satoshi Maeda, Mr. Masatoshi Yatago, Mr. Yuta Kobayashi, Mr. Takahito Endo, Ms. Ayana Yamamoto, Mr. Fumiya Ishizaka, Mr. Hiromu Fujimagari, Ms. Aya Onodera, Mr. Shogo Yanase, Mr. Hiroaki Kato, Mr. Toshihiro Wada, Mr. Yungoo Ro, Mr. Muye Chen, Mr. Yoshihiro Hiraya, Ryutaro Kodaira, Mr. Akihito Sonoda, Dr. Matthias T. Elm, Dr. Martin Fischer for their technical supports, valuable discussions and encouragement.

I would like to express my sincere thanks and appreciation to Dr. Hajime Goto, Dr. Natsuo Nakamura, and Dr. Takanori Maebashi for their invaluable discussions, support and encouragement.

I wish to say thanks for RCIQE researchers and students, Dr. Zenji Yatabe, Dr. Joel T. Asubar, Dr. Takashi Matsuda, Dr. Yuta Shiratori, Dr. Masafumi Tajima, Dr. Eri Ogawa, Dr. Chihoko Mizue, Dr. Keita Konishi, Dr. Kota Ohi, Mr. Takeshi Ejiri, Dr. Yujin Hori, Dr. Tomo Tanaka, Mr. Kensuke Miura, Mr. Hiroyuki Okazaki, Mr. Kazuhiro Takahagi, Mr. Naohisa Harada, Mr. Yuki Nakano, Mr. Toru Muramatsu, Mr. Yudai Imai, Mr. Tomohito Kudo, Mr. Shinya Okuzaki, Mr. Kenichiro Mori, Mr. Yuya Takatsuka, Mr. Satoshi Takeya, Mr. Taketsugu Ishikura, Mr. Zhixin Cui, Mr. Liumin Zou, Mr. Masaki Sato, Mr. Takayuki Tanaka, Mr. Naoki Azumaishi, Mr. Ryohei Jinbo, Mr. Yusuke Kumazaki, Mr. Takuma Nakano, Mr. Ryota Kuroda, Mr. Yuri Imai, Mr. Takahiro Hiraki, Mr. Lennart-Kund Liefeth, Mr. Yushi Abe, Mr. Shinya Inoue, Mr. Yutaka Senzaki, Mr. Takao Miyamoto, Mr. Akio Watanabe, Mr. Masahito Chiba, and Mr. Kenya Nishiguchi. And I also express thank for the other RCIQE students for their friendship.

I would like to extend my deepest gratitude to Mr. Kenji Takada, Ms. Satoko

Acknowledgement

Takeuchi, Ms. Mizuho Tanaka, Ms. Yuki Watanabe, Ms. Yuka Kamoto, and Ms Chieko Akiyama for their businesslike supports and encouragements.

Personally, I would like to express my sincere thanks to my grandparents, brother, and friends for their continual encouragement and support.

Finally, I really appreciate my parents, Hideo Sakita and Megumi Sakita. Their selfless support and encouragement always gives me energy, confidence and courage for my work and challenge. Thank you so much.

February 2016 at RCIQE, Shinya Sakita

Acknowledgement

Contents

Acknowledgements	i
Contents	v
Chapter 1 Introduction	1
1.1 Overview	1
1.1.1 Semiconductor Nanowire	2
1.1.2 Semiconductor Nanostructures on Glass Substrate	2
1.1.3 MnAs Nanoclusters	3
1.2 Outline of this thesis	5
Bibliography	7
Chapter 2 Experimental Technique	11
2.1 Metal-organic vapor phase epitaxy	11
2.2 Atomic layer deposition	15
2.3 Characterizations	16
Chapter 3 Crystallization of Al₂O₃	18
3.1 Phase transformation of bulk Al ₂ O ₃	18
3.2 Crystallization of Al ₂ O ₃ thin film prepared by ALD	21
3.3 Comparison of crystallization of Al ₂ O ₃ layers and AlGaAs growth on crystallized Al ₂ O ₃ layers deposited on Si (111) and amorphous glass substrates	22
Bibliography	29

Chapter 4	Growth of semiconducting nanowires on Al₂O₃/glass substrates	30
4.1	Introduction	30
4.2	Experimental procedure	31
4.3	Growth and structural characterization of AlGaAs nanostructures on crystallized Al ₂ O ₃ interlayers	34
4.4	Dependence of AlGaAs growth on Al ₂ O ₃ layer thickness	40
4.5	Selective-area growth of AlGaAs nanostructures on Al ₂ O ₃ /Si(111) substrate	44
4.6	Selective-area growth of AlGaAs nanostructures on amorphous glass substrate with crystallized Al ₂ O ₃ interlayers	46
4.7	Growth of nanowires on amorphous glass substrate with AlGaAs nanostructure buffers on crystallized Al ₂ O ₃ interlayers	48
4.8	Summary	51
	Bibliography	53
Chapter 5	MnAs/AlGaAs nanoclusters formed on Al₂O₃/Si(111) substrates	55
5.1	Introduction	55
5.2	Experimental procedure	57
5.3	Selective-area growth of MnAs/AlGaAs nanoclusters on Al ₂ O ₃ /Si(111)	59
5.4	Magnetic characterization by MFM observations	62
5.5	Leakage current measurement	63
5.6	Electrical characteristic of coupled MnAs nanocluster arrangement	64
	Bibliography	69

Chapter 6 Conclusion

71

List of publications

73

Chapter 1 Introduction

1.1 Overview

The field for nanotechnology represents an exciting and rapidly expanding research area including the physical, life, and engineering science. Much of the excitement in this area of research has arisen from recognition that new phenomena are possible with nanometer scale structures. These ideas have been motivated scientist to develop and sophisticate methods for making nanostructures.

Miniaturization of silicon electronics is being intensely pursued [1], although limitations in scaling, integration, and power consumption reduction will be difficult to achieve by the extension of current technologies, and thus a long-term approach for the investigation of novel-principle-based devices with new structures and new materials is essential. Bottom-up formation of semiconductor nanostructures has been attracted much attention. The use of nanoscale structures as building blocks for self-assembled [2–5] structures could potentially eliminate conventional and costly fabrication lines, while still maintaining some concepts that have proven successful in microelectronics. One-dimensional nanostructures, such as nanowires and carbon nanotubes, could be ideal building blocks for nanoelectronics [6], because they can function both as devices and as the wires that access them.

1.1.1 Semiconductor Nanowire

Bottom-up formation of vertical free-standing semiconductor nanowires has been continuously attracting much attention in the research fields of nanoelectronic and photonic devices, such as solar cells, lasers, light-emitting diodes, photodetectors, sensors, and transistors [7 - 10]. The typical approach of bottom-up growth of NWs, which has been developed worldwide, is the so-called vapor-liquid-solid (VLS) method using metal nanoparticles as a catalyst [11, 12]. To prevent the possible contamination of NWs by metal catalysts, in addition, the self-catalyzed [13 - 16] and oxide-assisted [17] growth of semiconductor NWs by the VLS or vapor-solid-solid (VSS) method has intensively been investigated as an alternative way. However, the VLS and VSS methods for NW growth still have problems to be solved for future nanoelectronic and photonic device applications because the NWs grown by the VLS and VSS methods are randomly distributed on the substrate and show a relatively low degree of size uniformity. We have developed the method of selective-area metal-organic vapor phase epitaxy (SA-MOVPE) for the catalyst-free growth of III-V compound semiconductor NWs [18 - 26]. It has been shown that the mechanism of NW growth by SA-MOVPE relies on the formation of crystal facets during the growth (the so-called faceting growth mode) [18, 19], not on the conventional self-catalyzed nor oxide-assisted growth modes. This method has a great advantage in terms of the controllability of the size and position of NWs on a semiconducting substrate.

1.1.2 Semiconductor Nanostructures on Glass Substrate

Recently, the growth of nanowires or nanostructures has been demonstrated on non-single-crystalline surface such as amorphous glass [27, 28], thermally oxidized SiO₂ layers, [29] and polycrystalline Si [30, 31]. In particular, amorphous glass is quite important and promising as a substrate for the realization of solar cells and light-emitting diodes on low-cost substrates as the eco-friendly green nanotechnologies because it is highly transparent, less toxic, much widely available, and cheaper than a conventional semiconducting substrate. However, the NWs directly grown on an amorphous glass substrate still have shown a relatively

poor controllability of their sizes, positions, directions, and shapes. Therefore, a pre-orienting film or a metal catalyst on an amorphous substrate is required for the nucleation to enhance the NW growth, as shown in previous studies [28, 29].

1.1.3 MnAs Nanoclusters

One approach comprises combining the advantages of semiconducting and magnetic properties. This is the aim in the field of spintronics, where not only the electron charge is actively utilized for the device performance but also the spin degree of freedom of the electron [31–34]. The combination of semiconducting and magnetic properties offers the possibility to obtain new functionalities compared to conventional semiconductor devices, such as non-volatility, higher speed, and lower power consumption, and may result in new multi-functional devices in the field of spin-electronics, spin-optoelectronics or quantum computing [13, 35–37]. Particularly, the intensive activities addressing the heteroepitaxy of ferromagnetic and III-V compound semiconducting layers (FM III-V hybrids) demonstrate the great interests of the semiconductor spintronics community in this subject. Due to the compatibility of these two types of materials in the hybrids, the possibility of generating new functionalities arises, which may form the basis for novel spintronic device concepts. Among all the FM III-V hybrids, the MnAs/GaAs materials system [38] has gained much attention because hexagonal NiAs-type MnAs layers and nanoclusters (NC) are ferromagnetic at room temperature or even higher temperatures [39, 40]. Magnetic logic operations were proposed using hexagonal NiAs-type MnAs thin films grown on GaAs (001) layers [41]. In addition, the ferromagnetic NiAs-type MnAs layers serve as an electrical spin injection source for semiconductors [42], and are used for lateral spin valve structures [43]. FM III-V hybrids are grown typically by molecular beam epitaxy at an extremely low growth temperature [44, 45], and devices are prepared on semiconducting substrates by using conventional top-down fabrication techniques. Granular hybrid structures in which ferromagnetic NCs are embedded into semiconductor layers are, in particular, an attractive candidate for the use in future nanospintronic devices because huge magnetoresistance (MR) effects were reported [46, 47].

However, the technological applications of these granular hybrids synthesized using such conventional techniques are mainly restricted to macroscopic devices. This is due to the random distribution of the NCs in the host material, e.g., the NC size and the randomness in the mean distance between the NCs, which possibly leads to statistical fluctuations in the device characteristics [47, 48]. This issue becomes more severe with increasing the degree of miniaturization and has to be solved in the future on the way towards miniaturized devices. In addition to the efforts of creating FM III-V hybrids, the MnAs thin films including poly-crystals, nanoparticles, and nanowires have also been investigated as candidates for possible spintronic device applications on Si [49-53]. We have developed an approach, the so called selective-area metal-organic vapor phase epitaxy (SA-MOVPE), where problems due to statistical fluctuations can be avoided. SA-MOVPE is based on the bottom-up formation of single-crystalline ferromagnetic MnAs NCs on defined sites of semiconducting substrates. The SA-MOVPE is promising as it enables us to accurately adjust the size, shape, number, position, and spatial arrangement of the MnAs NCs [54-57] within the hybrids to tune its magnetic and magnetotransport properties [41, 58-60]. Ordered planar arrangements of coupled NCs show large MR effects [61] and MR ratios of 300% are predicted by theory [62].

1.2 Outline of This Thesis

This thesis describes a series of experiments aimed at understanding and controlling semiconductor nanowire and ferromagnetic nanocluster growth formed on crystallized Al_2O_3 layers from the geometry shapes and crystal structures point of view, and clarification of growth mechanism of nanowires by selective area metal-organic vapor phase epitaxy.

This thesis divided into 6 chapters.

In chapter 2, detailed fabrication and characterization techniques of semiconducting nanowires and ferromagnetic nanoclusters are described. First, we describe overview of MOVPE growth including comparison of other growth techniques, growth process, MOVPE system, and growth characteristics. Second, principles of SA-MOVPE growth are explained. Next, the explanations of ordinary sample preparation for the semiconductor nanowires by SA-MOVPE are described. Finally, we explain characterization techniques that used for observing and imaging of structural information and investigation of optical properties of nanostructures.

In chapter3, I describe the mechanism of phase transformation of bulk or thin film of Al_2O_3 . Furthermore, we experimentally revealed crystal structure of Al_2O_3 layers deposited on Si(111) and amorphous glass substrate.

In chapter 4, we investigated the growth of nanowires and AlGaAs nanostructures on an amorphous glass substrate using the crystallization techniques of amorphous Al_2O_3 interlayers deposited by atomic layer deposition. First, we explain the experimental method. Then, we characterize AlGaAs nanostructures grown on the planar Al_2O_3 interlayers on the glass substrates. Crystal structure of Al_2O_3 layers prepared on glass substrate was characterized by cross-sectional lattice images. Finally, by using AlGaAs nanostructure buffers

in combination with the crystallized Al_2O_3 interlayers, we realize the nanowire formation tilted on the glass substrates.

In chapter 5, we investigated selective-area metal-organic vapor phase epitaxy and magnetic characterization of coupled MnAs/AlGaAs nanoclusters formed on thin Al_2O_3 insulating layers crystallized on Si (111) substrates. First, we explain the experimental method. Then, we characterized the crystal structure of crystallized Al_2O_3 grains, which are formed after an annealing treatment of the amorphous Al_2O_3 layers deposited by atomic layer deposition on Si (111) substrates. We observe that hexagonal MnAs nanoclusters on AlGaAs buffer layers grown by selective-area metal-organic vapor phase epitaxy on partially SiO_2 -masked Al_2O_3 insulator crystallized on Si (111) substrates. Next, we characterized magnetic domain structure of arrangements of coupled MnAs nanoclusters by magnetic force microscopy studies at room temperature. Finally we observed magnetic random telegraph noise, i.e. jumps between two discrete resistance levels, in a certain temperature range in such arrangements of coupled MnAs nanoclusters.

Summary and conclusions of the present work are shown and outlook for semiconducting nanowire and MnAs nanocluster fabrication are discussed in chapter 6.

Bibliography

- [1] Paul S. Peercy, *Nature* **406**, 1023 (2000).
- [2] H. Yan, H. S. Choe, S. W. Nam, Y. Hu, S. Das, J. F. Klemic, J. C. Ellenbogen, and C. M. Lieber, *Nature* **470**, 240 (2011).
- [3] R. Yan, D. Gargas, and P. Yang, *Nat. Photonics* **3**, 569 (2009).
- [4] J. Wallentin, N. Anttu, D. Asoli, M. Huffman, I. Åberg, M. H. Magnusson, G. Siefer, P. Fuss-Kailuweit, F. Dimroth, B. Witzigmann, H. Q. Xu, L. Samuelson, K. Deppert, and M. T. Borgström, *Science* **339**, 1057 (2013).
- [5] Y. Cui, Q. Wei, H. Park, and C. M. Lieber, *Science* **293**, 1289 (2001).
- [6] C. B. Murray, C. R. Kagan, M. G. Bawendi, *Science* **270**, 1335 (1995).
- [7] H. Yan, H. S. Choe, S. W. Nam, Y. Hu, S. Das, J. F. Klemic, J. C. Ellenbogen, and C. M. Lieber, *Nature* **470**, 240 (2011).
- [8] R. Yan, D. Gargas, and P. Yang, *Nat. Photonics* **3**, 569 (2009).
- [9] J. Wallentin, N. Anttu, D. Asoli, M. Huffman, I. Åberg, M. H. Magnusson, G. Siefer, P. Fuss-Kailuweit, F. Dimroth, B. Witzigmann, H. Q. Xu, L. Samuelson, K. Deppert, and M. T. Borgström, *Science* **339**, 1057 (2013).
- [10] Y. Cui, Q. Wei, H. Park, and C. M. Lieber, *Science* **293**, 1289 (2001).
- [11] K. Hiruma, M. Yazawa, T. Katsuyama, K. Ogawa, K. Haraguchi, M. Koguchi, and H. Kakibayashi, *J. Appl. Phys.* **77**, 447 (1995).
- [12] Y. Wang, V. Schmidt, S. Senz, and U. Gösele, *Nat. Nanotechnol.* **1**, 186 (2006).
- [13] B. Mandl, J. Stangl, E. Hilner, A. A. Zakharov, K. Hillerich, A. W. Dey, L. Samuelson, G. Bauer, K. Deppert, and A. Mikkelsen, *Nano Lett.* **10**, 4443 (2010).
- [14] F. Jabeen, V. Grillo, S. Rubini, and F. Martelli, *Nanotechnology* **19**, 275711 (2008).
- [15] Y. Cohin, O. Mauguin, L. Largeau, G. Patriarche, F. Glas, E. Søndergaard J. C. Harmand, *Nano Lett.* **13**,

2743 (2013).

[16] M. R. Ramdani, J. C. Harmand, F. Glas, G. Patriache, and L. Travers, *Cryst. Growth Des.* **13**, 91 (2013).

[17] S. Noor Mohammad, *J. Vac. Sci. Technol. B* **26**, 1993 (2008).

[18] K. Ikejiri, J. Noborisaka, S. Hara, J. Motohisa, and T. Fukui, *J. Cryst. Growth* **298** (2007) 616.

[19] K. Ikejiri, T. Sato, H. Yoshida, K. Hiruma, J. Motohisa, S. Hara, and T. Fukui, *Nanotechnology* **19** (2008) 265604.

[20] Y. Kohashi, S. Hara, and J. Motohisa, *Mater. Res. Express* **1** (2014) 015036.

[21] S. Hara, S. Sakita, and M. Yatago, *Jpn. J. Appl. Phys.* **51** (2012) 11PE01.

[22] B. Hua, J. Motohisa, Y. Kobayashi, S. Hara, and T. Fukui, *Nano Lett.* **9** (2008) 112..

[23] K. Tomioka, J. Motohisa, S. Hara, K. Hiruma, and T. Fukui, *Nano Lett.* **10** (2010) 1639.

[24] T. Tanaka, K. Tomioka, S. Hara, J. Motohisa, E. Sano, and T. Fukui, *Appl. Phys. Express* **3** (2010) 025003.

[25] S. Maeda, K. Tomioka, S. Hara, and J. Motohisa, *Jpn. J. Appl. Phys.* **51**, 02BN03 (2012).

[26] Y. Kobayashi, Y. Kohashi, S. Hara, and J. Motohisa, *Appl. Phys. Express* **6**, 045001 (2013).

[27] J. H. Choi, A. Zoukarnееv, S. I. Kim, C. W. Baik, M. H. Yang, S. S. Park, H. Suh, U. J. Kim, H. B. Son, J. S. Lee, M. Kim, J. M. Kim, and K. Kim, *Nat. Photonics* **5**, 763 (2011).

[28] V. Dhaka, T. Haggren, H. Jussila, H. Jiang, E. Kauppinen, T. Huhtio, M. Sopanen, and H. Lipsanen, *Nano Lett.* **12**, 1912 (2012).

[29] X. Sun, G. Calebotta, B. Yu, G. Selvaduray, and M. Meyyappan, *J. Vac. Sci. Technol. B* **25**, 415 (2007).

[30] K. Ikejiri, F. Ishizaka, K. Tomioka, and T. Fukui, *Nanotechnology* **24**, 115304 (2013).

[31] K. W. Ng, T. T. D. Tran, W. S. Ko, R. Chen, F. Lu, and C. J. Chang-Hasnain, *Nano Lett.* **13**, 5931 (2013).

[32] G. A. Prinz, *Science*, **282**, 1660 (1998).

[33] H. Ohno, *Science*, **281**, 951 (1998).

[34] S. A. Wolf, D. D. Awschalom, R. A. Buhrman, J. M. Daughton, S. von Molnár, M. L. Roukes, A. Y.

- Chtchelkanova , D. M. Treger , Science, **294**, 1488 (2001).
- [35] M. Tanaka , J. Cryst. Growth, **278**, 25 (2005).
- [36] H. Katayama-Hoshida , K. Sato , T. Fukushima , M. Toyoda , H. Kizaki , V. A. Dinh , P. H. Dederichs , P
hys. Status Solidi A, **204**, 3 (2007).
- [37] D. D. Awschalom , M. E. Flatte , Nat. Phys., **3**, 153 (2007).
- [38] C. Gould , K. Pappert , G. Schmidt , L. W. Molenkamp , Adv. Mater., **19**, 323 (2007).
- [39] R. Engel-Herbert, T. Hesjedal, D. M. Schaadt, L. Däweritz, and K. H. Ploog, Appl. Phys. Lett. **88**,
052505 (2006).
- [40] F. Ishikawa, K. Koyama, K. Watanabe, and H. Wada, Jpn. J. Appl. Phys. **42**, L918 (2003).
- [41] M. T. Elm, C. Michel, J. Stehr, D. M. Hofmann, P. J. Klar, S. Ito, S. Hara, and H.-A. Krug von Nidda, J.
Appl. Phys. **107**, 013701 (2010).
- [42] P. Pampuch, A. K. Das, A. Ney, L. Däweritz, R. Koch, and K. H. Ploog, Phys. Rev. Lett. **91**, 147203
(2003).
- [43] M. Ramsteiner, H. Y. Hao, A. Kawaharazuka, H. J. Zhu, M. Kästner, R. Hey, L. Däweritz, H. T. Grahn,
and K. H. Ploog: Phys. Rev. B **66**, 081304(R) (2002).
- [44] D. Saha, M. Holub, P. Bhattacharya, and Y. C. Liao: Appl. Phys. Lett. **89**, 142504 (2006).
- [45] V. Garcia, H. Jaffrès, J.-M. George, M. Marangolo, M. Eddrief, and V. H. Etgens, Phys. Rev. Lett. **97**,
246802 (2006).
- [46] S. Sugahara and M. Tanaka, Appl. Phys. Lett. **80**, 1969 (2002).
- [47] P. N. Hai, S. Ohya, M. Tanaka, S. E. Barnes, and S. Maekawa, Nature **458**, 489 (2009).
- [48] C. Michel, M. T. Elm, B. Goldlücke, S. D. Baranovskii, P. Thomas, W. Heimbrodtt, and P. J. Klar, Appl.
Phys. Lett. **92**, 223119 (2008).
- [49] K. Akeura, M. Tanaka, T. Nishinaga, and J. De Boeck, J. Appl. Phys. **79**, 4957 (1996).
- [50] A. M. Nazmul, A. G. Banskchikov, H. Shimizu, and M. Tanaka, J. Cryst. Growth **227-228**, 874 (2001).
- [51] M. Solzi, C. Pernechele, M. Ghidini, M. Natali, and M. Bolzan, J. Magn. Magn. Mater. **322**, 1565

(2010).

[52] M. F. H. Wolff, D. Görlitz, K. Nielsch, M. E. Messing, and K. Deppert, *Nanotechnology* **22**, 055602

(2011).

[53] J. Sadowski, A. Siusys, A. Kovacs, T. Kasama, R. E. Dunin-Borkowski, T. Wojciechowski, A. Reszka, and B. Kowalski, *Phys. Status Solidi B* **248**, 1576 (2011).

[54] S. Hara, D. Kawamura, H. Iguchi, J. Motohisa, and T. Fukui, *J. Cryst. Growth* **310**, 2390 (2008).

[55] S. Ito, S. Hara, T. Wakatsuki, and T. Fukui, *Appl. Phys. Lett.* **94**, 243117 (2009).

[56] K. Komagata, S. Hara, S. Ito, and T. Fukui, *Jpn. J. Appl. Phys.* **50**, 06GH01 (2011).

[57] S. Hara and K. Komagata, *Phys. Status Solidi B* **252**, 1925 (2015).

[58] M. T. Elm, P. J. Klar, S. Ito, and S. Hara, *Phys. Rev. B* **83**, 235305 (2011).

[59] M. T. Elm, P. J. Klar, S. Ito, S. Hara, and H.-A. Krug von Nidda, *Phys. Rev. B* **84**, 035309 (2011).

[60] M. Fischer, M. T. Elm, H. Kato, S. Sakita, S. Hara, and P. J. Klar, *Phys. Rev. B* **92**, 165306 (2015).

[61] M. Fischer, M. T. Elm, S. Sakita, S. Hara, and P. J. Klar, *Appl. Phys. Lett.* **106**, 032401 (2015).

[62] C. Heiliger, M. Czerner, P. J. Klar, and S. Hara, *IEEE Trans. Magn.* **46**, 1702 (2010).

Chapter 2 Experimental Technique

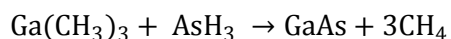
2.1 Metal-Organic Vapor Phase Epitaxy

In this study, MnAs nanoclusters are formed by selective-area MOVPE which is one of the bottom-up techniques. This fabrication technique uses masked substrate as a template of crystal growth and brings well-controlled nanowire arrays.

MOVPE technique is used for realizing single crystalline thin-films as one of the methods of chemical vapor deposition. Especially, the III-V compound semiconductor films such as GaAs, InP, InAs and their ternary alloys are fabricated by MOVPE. III and V metal-organic and source gases are used for growing compound semiconductors and II and IV elements for p-type and n-type doping are used. Especially, bold face elements in Fig. 3-1 are used for this study for fabricating of III-V compound semiconductors with p-n junctions. This technique can be controlled atomic composition of mixed crystal semiconductors by partial pressures of supplying sources, and steep heterojunctions or p-n junctions can be formed by precise control of source gas flow. Additionally, MOVPE method has the potential for high-volume production with uniformly growth of semiconductor layer at once and commercially uses for fabrication of semiconductor devices.

In this technique, the source materials for III-V compound semiconductor growth are provided with purified hydrogen gas and diffuse near the surface of the substrate. Then, these molecules react chemically in the surface of growth substrate which is heated and epitaxial layer occurs at the surface of substrate in

relationship to the underlying crystal structure. In the case of GaAs layer growth, trimethylgallium (TMGa: Ga(CH₃)₃) and arsine (AsH₃) are used, and epitaxial film of GaAs can grow according to the following reaction.



II	III	IV	V
	Boron 5 B	Carbon 6 C	Nitrogen 7 N
	Aluminum 13 Al	Silicon 14 Si	Phosphorus 15 P
Zinc 30 Zn	Gallium 31 Ga	Germanium 32 Ge	Arsenic 33 As
Cadmium 48 Cd	Indium 49 In	Tin 50 Sn	Antimony 51 Sb

Fig. 2-1 The periodic table from II to V elements. The elements used in this study are indicated by boldface for III-V compound semiconductors and impurity doping.

MOVPE growth process

In this study, epitaxy is carried out in a horizontal MOVPE system with 3.0 slm of the total gas flow rate, and the system is working at 0.1atm. The system consists of a gases delivery system, exhaust disposal system, and a reactor system with temperature controller [Fig. 3-2].

The gases delivery system consists of lines, bubblers, valves and mass flow controllers (MFCs). The MO sources are provided in bubblers as shown in Fig. 3-3. Pressure control valve maintains the pressure of bubbler at 760 Torr. The carrier gas of palladium diffused purified hydrogen is led through source materials in the bubbler. We can control vapor pressure of the metal organic sources by the combination of thermal bath temperature and MFCs in each line of bubblers. And gas sources are provided from gas cylinders (in

this study, AsH_3 and SiH_4). During the epitaxial growth, MO and gas sources are transported to the reactor in each run lines with hydrogen carrier gas.

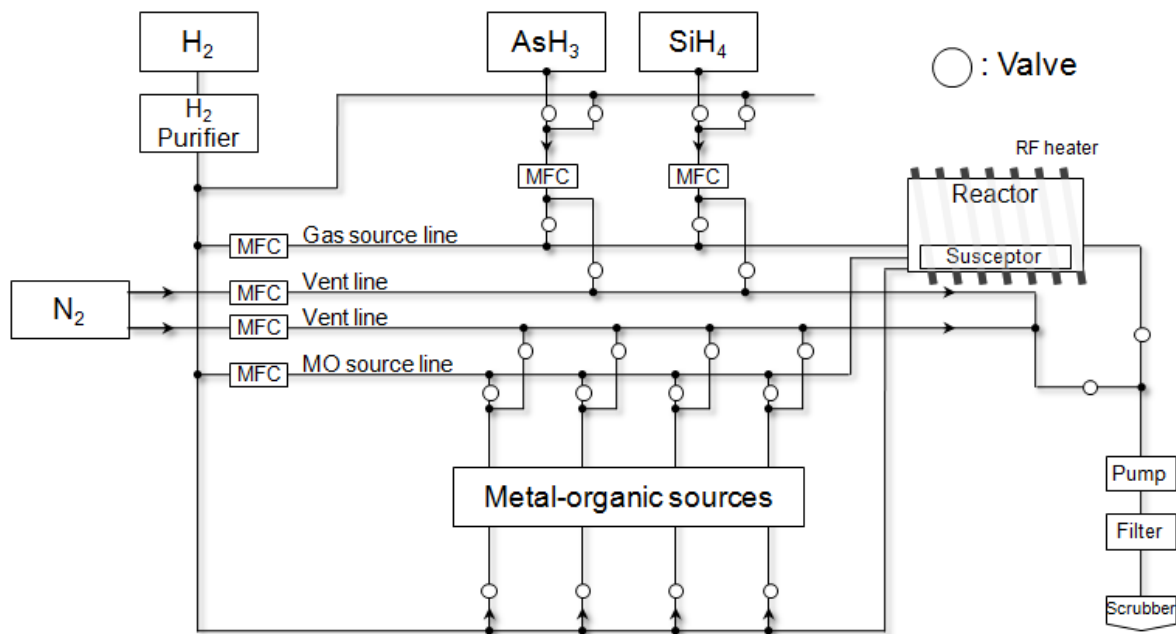


Fig. 2-2 Schematic illustration of the MOVPE system for III-V compound semiconductor nanowires in this study.

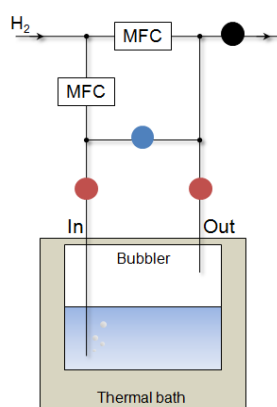


Fig. 2-3 Schematic illustration of metalorganic sources provided by bubblers. Black valve indicates the pressure control valve.

The exhaust disposal system consists of exhaust lines and rotary pump to maintain the reactor at low pressure. These are connected to exhaust toxic gas treatment system because toxic gases are used as the source materials in MOVPE.

The reactor system consists of a quartz reactor, a quartz tray, a carbon susceptor and radio frequency (RF) heater. The flow dynamics for crystal growth in MOVPE technique are divided into 4 general phases: mass and heat transport, physical surface processes, chemical reactions, and thermodynamics. Especially, in the mass and heat transport phase, a boundary layer above the growing surface is formed by the laminar flow of the vapor in the reactor, and the source materials are transported to the surface of the growth substrate [Fig. 3-4]. The thickness of boundary layer is increasing related to the square root of the distance from front edge of susceptor.

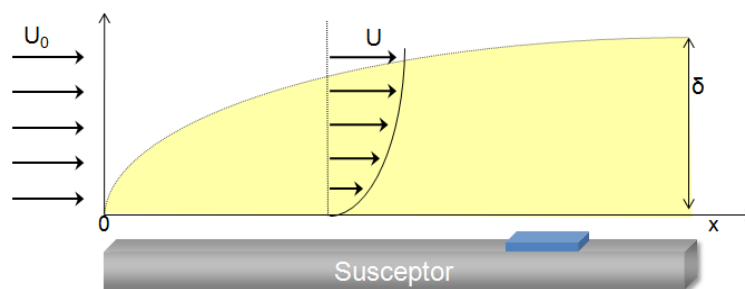


Fig. 2-4 Schematic illustration of boundary layer above the susceptor in the reactor. (δ : boundary layer thickness, U : velocity of the gas)

2.2 Atomic Layer Deposition

Atomic Layer Deposition (ALD) is a technique that allows deposition of thin films, atomic layer by layer. ALD is based on the sequential injection of each chemical, leading to a monolayer-level deposition. The typical ALD reaction is illustrated via the formation of Al_2O_3 from trimethylaluminum or TMA, $\text{Al}(\text{CH}_3)_3$, and water, H_2O . Fundamental deposition mechanism is explained below and Fig. 2-5.

Step 1: Introduction and adsorption of precursor A to the surface. The precursor, trimethylaluminum reacts with hydroxyl groups on the surface of the substrate, liberating methane. The reaction is self-limiting as the precursor does not react with adsorbed aluminum species.

Step 2: Removal of the unreacted precursor and reaction products. Unreacted precursor and the methane (CH_4) liberated from the reaction are removed by simple evacuation of the sample chamber or by flowing inert gas over the surface.

Step 3: Introduction and adsorption of precursor B to the surface. Water reacts with the methyl groups on the deposited aluminum atoms forming both Al-O-Al bridges, as well as new hydroxyl groups. The formation of hydroxyl groups readies the surface for the acceptance of the next layer of aluminum atoms. Methane is liberated as a by-product. By the GaAs growth using the crystallization technique of Al_2O_3 interlayers and AlGaAs nanostructure

Step 4: Removal of the unreacted precursor and reaction products via evacuation and/or inert gas flow.

Step 5: Repeat to create layers. The process begins again with the introduction of precursor A followed by B. Atomic layers are built up one after the other.

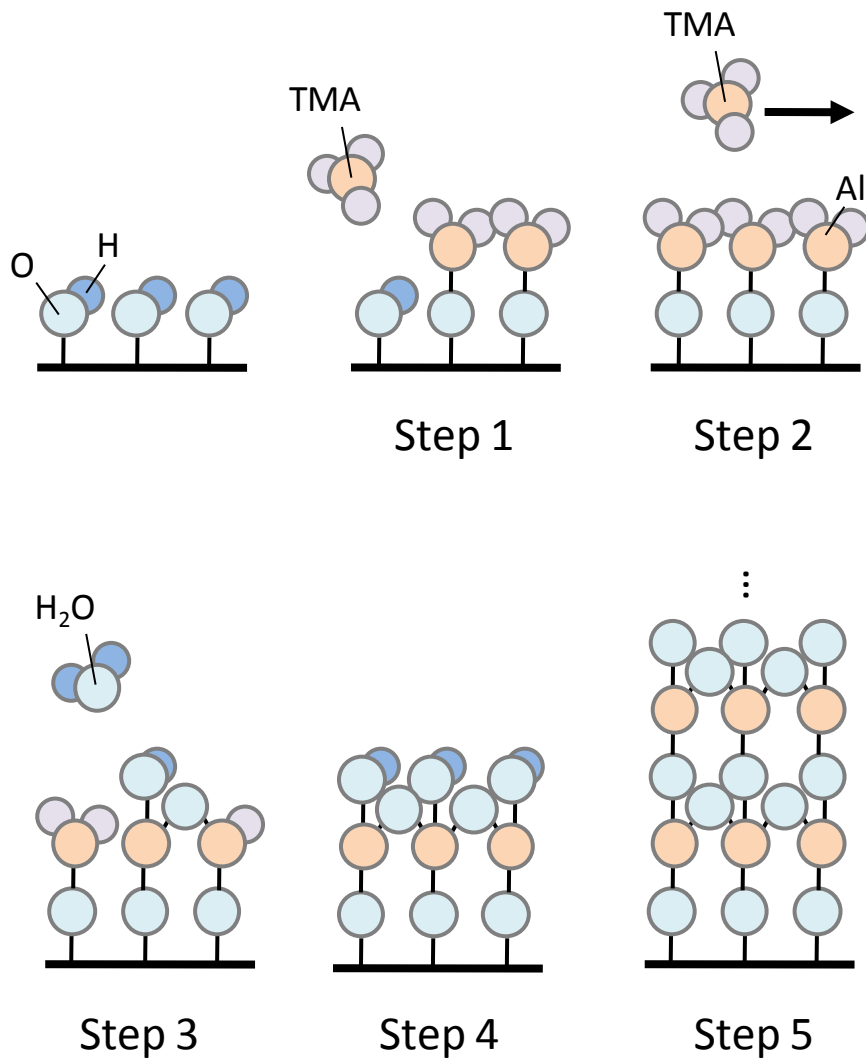


Fig. 2-5 Schematic illustrations of the ALD reactions for the deposition of the Al_2O_3 .

2.3 Characterizations

Scanning electron microscopy

Scanning electron microscopy (SEM) is used for structural characterization of grown nanowires or the results of fabrication process for nano-devices in this study (Hitachi hitec: SU-8010). The general system consists of an electron gun, condenser lenses, scanning coils, an objective lens, and detector for secondary electron. The electron beam is finely focused by a set of these lenses and scanning coil, and the image is

generated by scanning over the sample. The screening and detection of secondary electron which is emitted by the surface of the target shows the valuable information about the surface morphology and geometrical features of the nanowires

Magnetic force microscopy

The magnetic force microscope (MFM) is a variety of atomic force microscope, where a sharp magnetized tip scans a magnetic sample; the tip-sample magnetic interactions are detected and used to reconstruct the magnetic structure of the sample surface. Many kinds of magnetic interactions are measured by MFM, including magnetic dipole–dipole interaction. MFM scanning often uses non-contact AFM (NC-AFM) mode.

Chapter 3 Crystallization of Al₂O₃

3.1 Phase Transformation of Bulk Al₂O₃

According to Ref. [1], Al₂O₃ exists in many metastable polymorphs besides the thermodynamically stable α -Al₂O₃ (corundum form). The metastable Al₂O₃ structures can be divided into two broad categories: a face-centered cubic (fcc) or a hexagonal close-packed (hcp) arrangement of oxygen anions. It is the distribution of cations within each subgroup that results in the different polymorphs.¹ The Al₂O₃ structures based on fcc packing of oxygen include γ , η (cubic), υ (monoclinic), and δ (either tetragonal or orthorhombic), whereas the Al₂O₃ structures based on hcp packing are represented by the α (trigonal), κ (orthorhombic), and ξ (hexagonal) phases.

Because of their fine particle size, high surface area, and catalytic activity of their surfaces, the transition aluminas (especially the γ form) find applications in industry as adsorbents, catalysts or catalyst carriers, coatings, and soft abrasives. The excellent stoichiometry and stability of Al₂O₃ help to make it an important constituent of many protective oxide scales formed on the surface of high-temperature metals and alloys. The dominant (and stable) phase in these scales is α -Al₂O₃, whose occurrence also dominates the adhesion and coherence of the scale. Heat treatments designed to promote stable scale formation depend on an understanding of the metastable intermediate polymorphic structures and the transformation mechanisms that result in the formation of α -Al₂O₃. An understanding of the mechanisms of polymorphic phase transformations also is of major importance for the sintering of nanosized Al₂O₃ powders, which are usually

γ -Al₂O₃ but transform during sintering to α - Al₂O₃. Both the sintering and the grain growth behavior are related strongly to this phase transformation. Extensive research has been reported over the past few decades characterizing the transition aluminas with respect to dehydroxylation and the transformation mechanisms, porosity and specific surface area, surface structure and chemical reactivity, and the defect crystal structure. However, poorly developed crystallinity and possible surface-energy stabilization have made it difficult for advanced surface analytical techniques to probe such fine and irregular structures, and singlecrystal X-ray diffractometry (XRD) from such poorly ordered structures is not feasible. The main tools used for the analysis of the Al₂O₃ polymorphs were, therefore, powder XRD and selected-area electron diffraction (SAD). Both methods suffer from serious disadvantages when applied in isolation to such complicated structures as the transition aluminas. These structures have very similar *d*-spacings, which makes difficult the precise solution of the structure by XRD, especially because the transformations appear to be continuous during heating, with several phases coexisting in the samples. Moreover, the phase transformations in Al₂O₃ are accompanied by changes in symmetry that lead to a number of variants for both δ - and ν - Al₂O₃. It is impossible to include such detailed information in polycrystal X-ray structure analysis, where the structure is “averaged” over many crystals. Conventional transmission electron microscopy (TEM) can clarify some of these problems, but, unfortunately, electron diffraction contrast does not provide information about the atomic positions in a crystal structure. On the other hand, high-resolution electron microscopy (lattice imaging) can reveal the crystallographic relations between the phases and allows the atomic structure to be determined through a comparison of the experimental images with those calculated by computer simulation. Lattice imaging of the interfaces between the Al₂O₃ polymorphs can provide additional information about the transformation mechanisms. However, until very recently, little high-resolution work on the polymorphic phase transformations in Al₂O₃ has been reported, and, as a result, the structure of most transition aluminas has not been finally determined, nor are the mechanisms of the polymorphic phase transformations understood. The most comprehensive review of Al₂O₃ polymorphs is that presented by Wefers and Misra [1] in 1987. Since then, many studies that have used modern experimental and theoretical methods have reported

on different aspects of polymorphism in Al₂O₃. The goal of the present contribution is to provide an updated review of the known metastable Al₂O₃ structures and to summarize the current understanding of the mechanisms involved in a number of the phase transformations.

Metastable Al₂O₃ phases commonly are obtained by one of the processing routes summarized in Table I. Differences in the phase transformation sequence usually are ascribed to differences in the precursor structure [2, 3]. The temperature ranges of stability given for the transition aluminas are only approximate and depend, among other things, upon the degree of crystallinity, the presence of impurities in the starting materials, and the subsequent thermal history. All the phases observed in the transition aluminas are reproducible and remain stable at room temperature, but the sequence of transformations is not reversible when the temperature is decreased [1]. The sequences of the phase transformations reported in the literature on passing from the metastable Al₂O₃ structures to the final stable α -Al₂O₃ phase also are approximate. For example, no direct experimental evidence has confirmed the existence of a direct $\delta \rightarrow \upsilon$ transformation or disproved a direct $\gamma \rightarrow \alpha$ transformation

hcp
α -AlOOH (diaspore) — (700-800°C) → α -Al ₂ O ₃ γ -Al(OH) ₃ — (150-300°C) → χ — (650-750°C) → κ — (1000°C) → α -Al ₂ O ₃ 5Al ₂ O ₃ ·H ₂ O (tohdite) — (700-800°C) → κ' — (750°C) → κ — (900°C) → α -Al ₂ O ₃ Vapor (CVD) → κ → α -Al ₂ O ₃
fcc
γ AlOOH (boehmite) — (300-500°C) → γ — (700-800°C) → δ — (900-1000°C) → θ — — (1000-1100°C) → α -Al ₂ O ₃ α -Al(OH) ₃ (bayerite) — (200-300°C) → η — (600-800°C) → θ — (1000-1100°C) → α -Al ₂ O ₃ Amorphous (anodic film) → γ → δ → θ → α -Al ₂ O ₃ Melt → γ → δ, θ → α -Al ₂ O ₃

Table 1 Common processing routes resulting in formation of different metastable Al₂O₃ structures and the sequences phase transformations toward the stable α -Al₂O₃ phase.

3.2 Crystallization of Al₂O₃ thin film prepared by atomic layer deposition

It has been reported that thin amorphous Al₂O₃ layers deposited by ALD are crystallized after the anneal treatment at a relatively high temperature [6 - 8]. Furthermore, the epitaxial growth of semiconductors on Al₂O₃ layers deposited on single-crystalline substrates by ALD has been demonstrated, e.g., GaN growth on Si (111) substrate and InGaN growth on ZnO (0001) substrate with the Al₂O₃ interlayers [9, 10].

3.3 Comparison of crystallization of Al₂O₃ layers and AlGaAs growth on crystallized Al₂O₃ layers deposited on Si (111) and amorphous glass substrates

We conducted the crystallization of Al₂O₃ layers deposited by ALD and AlGaAs growth experiments in order to characterize surface morphologies and/or crystal structures of AlGaAs and Al₂O₃ on Si (111) and amorphous glass substrates.

AlGaAs nanostructures were grown on Al₂O₃ layers deposited by ALD on amorphous glass, which was synthetic quartz, AQ series, manufactured by ASAHI GLASS Co. Ltd., and Si (111) substrates. First, we deposited thin amorphous Al₂O₃ layers by ALD on both Si (111), which was etched by hydrofluoric acid (HF) before the use, and amorphous glass substrates, as illustrated in Fig. 1(a). We annealed the samples for crystallizing the amorphous Al₂O₃ layers in the MOVPE reactor, and then, finally, AlGaAs nanostructures were grown by MOVPE on the substrate. Al₂O₃ layers with the thickness of 5 to 20 nm were deposited at the temperature of 300 °C with (CH₃)₃Al and H₂O as the precursors in the ALD system. The annealing temperature and time for the crystallization experiments of the Al₂O₃ layers were 975 °C and 10 minutes in H₂ atmosphere in the MOVPE reactor. For the MOVPE growth of AlGaAs nanostructures, (CH₃)₃Ga, (CH₃)₃Al, and 20%-AsH₃ diluted in H₂ were used as source materials. The estimated partial pressures of (CH₃)₃Ga, (CH₃)₃Al, and AsH₃ in the MOVPE reactor were approximately [(CH₃)₃Ga] = 2.0 × 10⁻⁶, [(CH₃)₃Al] = 3.3 × 10⁻⁷, and [AsH₃] = 1.2 × 10⁻³ atm, respectively. After the annealing at 975 °C for 10 minutes in H₂ atmosphere before the AlGaAs growth, only H₂ was introduced into the MOVPE reactor during the decrease in temperature to the growth temperature, T_g, for AlGaAs. AlGaAs was grown first at a relatively low T_g of 400 °C for 3 minutes as buffer layers, and then at T_g of 750 °C for 10 minutes. Scanning electron microscopy (SEM) was used for the observations of AlGaAs nanostructures and surface morphologies, and transmission electron microscopy (TEM) was used for the structural characterization in detail by the cross-sectional lattice images of AlGaAs

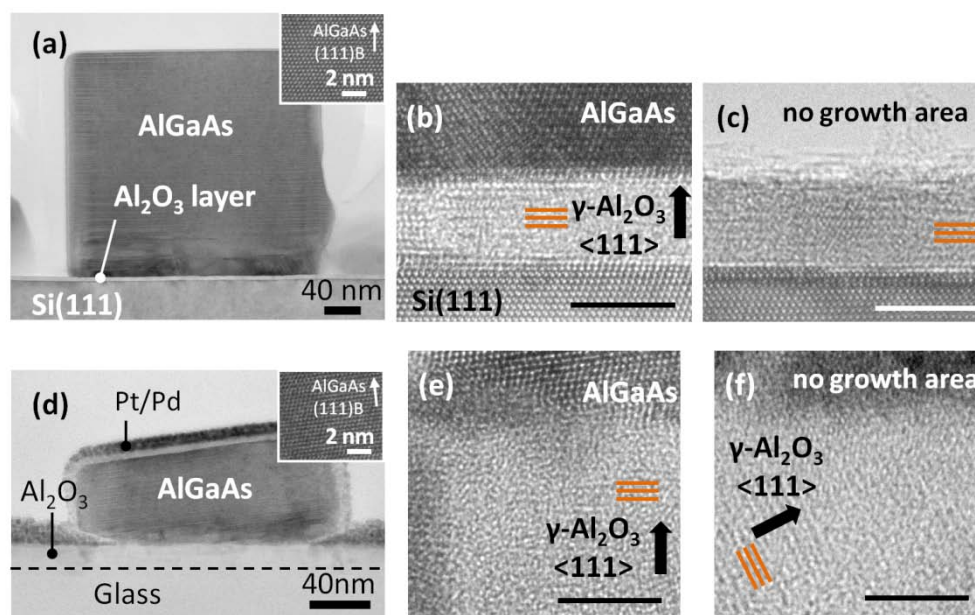


Fig. 5-4 Cross-sectional TEM images: (a) and (d) for a typical hexagonal AlGaAs nanostructure, (b) and (e) for lattice images of Al₂O₃ layers under the hexagonal AlGaAs nanostructures of (a) and (d), (c) and (f) for lattice images of Al₂O₃ layers in no AlGaAs growth area on the Al₂O₃ layers. (a) to (c) are on 5-nm-thick Al₂O₃ layers on Si(111) substrate, and (d) to (f) are on 20-nm-thick Al₂O₃ layers on an amorphous glass substrate. The insets of (a) and (d) show lattice images of AlGaAs nanostructures. White or black scale bars in (b), (c), (e), and (f) represent 5 nm. Electron-beam injection was perpendicular to one of the side-wall planes of AlGaAs hexagonal prisms.

nanostructures and Al₂O₃ layers. To observe AlGaAs nanostructures and Al₂O₃ layers on an amorphous glass substrate by SEM, conductive Pt/Pd thin films were deposited by ion sputtering after the AlGaAs growth because a glass substrate is an insulator. We also used X-ray diffraction (XRD) for the structural characterization of AlGaAs nanostructures.

We first observed by TEM crystal structures of Al₂O₃ layers on Si (111) and amorphous glass substrates. Figure 4(a) shows cross-sectional TEM images using an electron-beam injection perpendicular to one of the side-wall crystal facets, i.e. {0-11}, of hexagonal AlGaAs nano-pillars or NWs grown on 5-nm-thick Al₂O₃ layers on Si (111) substrate. Al₂O₃ layers in some areas, including under the hexagonal AlGaAs nano-pillars (Fig. 4(b)) and around the areas with no AlGaAs growth (Fig. 4(c)), were also observed in detail by high-resolution TEM. It was confirmed that lattice fringes were markedly observed in wide areas in the Al₂O₃ layers, and that they were approximately parallel to the Si (111) substrate planes. It was

estimated by the fast Fourier transform, or FFT, from the observed lattice images that these lattice fringes were attributable to the lattice spacing of 0.46 nm, and that it was in good agreement with the well-known literature value of 0.456 nm for the {111} planes of γ -Al₂O₃ (from the JCPDS database). Therefore, it was reasonable that the crystal structure of crystal grains observed in the Al₂O₃ layers was γ -Al₂O₃, and that the $\langle 111 \rangle$ direction of γ -Al₂O₃ layers was parallel to the Si $\langle 111 \rangle$ direction. From high-resolution TEM observations for the Al₂O₃ layers, as shown in Figs. 4(e) and (f), lattice fringes of γ -Al₂O₃ $\langle 111 \rangle$ direction were observed, as in the case of the Al₂O₃ layers on Si (111) substrates. Some of the γ -Al₂O₃ {111} planes were parallel to the glass substrate surface, whereas others were tilted against the substrate. Therefore, we concluded that the crystallized γ -Al₂O₃ layers were a polycrystalline.

It is possible that the γ -phase Al₂O₃ crystal grains have been formed as a stable phase in amorphous Al₂O₃ layers in the current work. For the oriented crystallization in amorphous Al₂O₃ layers on Si (111) substrates, an effective lattice mismatch between Si (111) and γ -Al₂O₃ {111} planes, which was estimated to be about 2.9% in Ref. [26], and which was much smaller than the actual cubic-cubic lattice mismatch of 45% between them, might play an important role in our samples. Crystallization characteristics of α - and γ -Al₂O₃ layers on single-crystalline Si (111) and 4H-SiC (0001) substrates after the annealing of ALD-deposited amorphous Al₂O₃ layers were investigated in Refs. [6, 7], respectively, and it was shown that there was a marked epitaxial relationship between γ -Al₂O₃ {111} layers and the substrates. Therefore, it appeared that the amorphous Al₂O₃ layers were epitaxially crystallized as γ -phase Al₂O₃ crystal grains on Si (111) substrates in the current work. On the other hand, in the case of the samples on an amorphous glass substrate, some of the γ -Al₂O₃ crystal grains with tilted crystal axes were formed possibly because no epitaxial crystallization occurred in the amorphous Al₂O₃ layers.

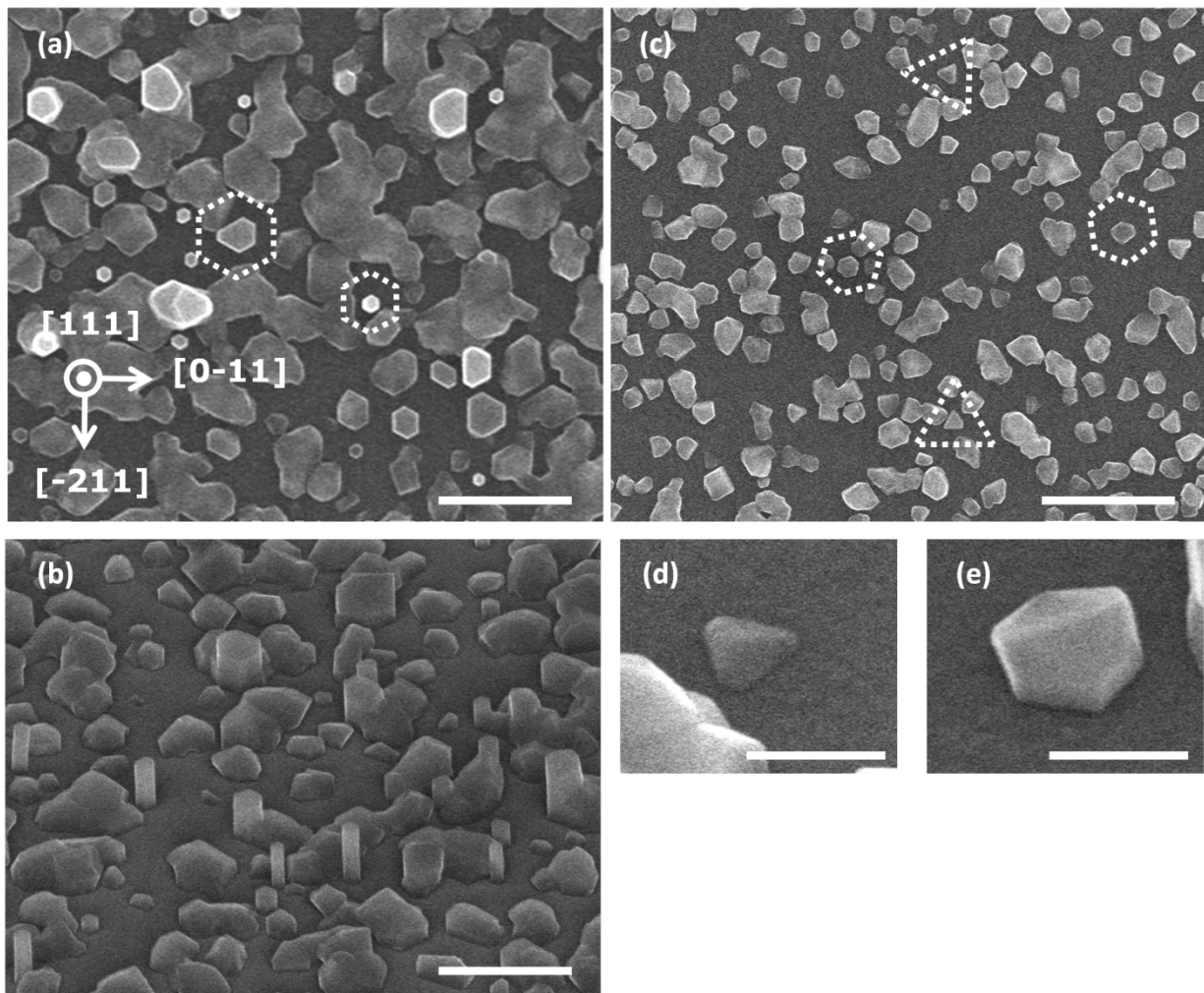


Fig. 5-4 SEM images of AlGaAs nanostructures on 5-nm-thick Al_2O_3 layers deposited on (a) and (b) Si (111) substrate, and (c), (d), and (e) amorphous glass substrate. (a) and (c) are the top views of SEM images, and (b), (d), and (e) are the bird's-eye views. (d) and (e) are highly-magnified SEM images for typical structures with a tetrahedral and hexagonal shape, respectively. White scale bars represent 1 μm in (a) to (c), and 200 nm in (d) and (e), respectively.

Next, we observed by SEM the differences in surface morphologies of AlGaAs nanostructures grown on 5-nm-thick planar Al_2O_3 layers on Si (111) and amorphous glass substrates. The substrates for the AlGaAs growth were as shown in Fig. 1(a). Figures 2(a) and (b) show top and bird's-eye views of SEM images for the AlGaAs nanostructures on 5-nm-thick planar Al_2O_3 layers on Si (111) substrate, respectively. White scale bars represent 1 μm in Figs. 2(a) and (b). We observed that AlGaAs nano-pillars, or NWs, with a hexagonal prism shape and a relatively high-aspect ratio, i.e. the height of around 300 nm and the diameter of

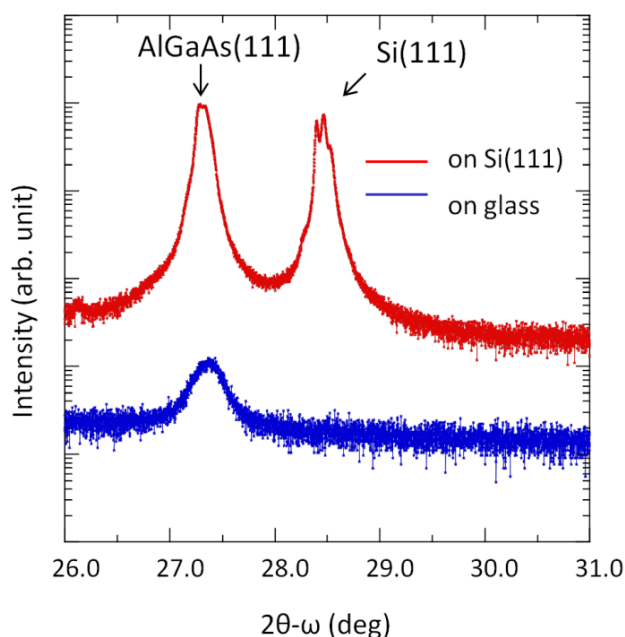


Fig. 5-4 XRD rocking curves in logarithmic scale for the samples on Si (111) and amorphous glass substrates observed in Fig. 2.

50 to 500 nm, were partly formed. The side-wall crystal facets of most of the hexagonal nano-pillars were parallel to the $\{-110\}$ planes of Si (111) substrate, as indicated by white broken-lined hexagons in the Fig. 2(a). Polycrystalline AlGaAs nanostructures were also randomly formed on the Al₂O₃ surfaces. Figure 2(c), next, shows a typical SEM top view of AlGaAs nanostructures on 5-nm-thick planar Al₂O₃ layers deposited on an amorphous glass substrate. Highly-magnified SEM bird's-eye views of AlGaAs nanostructures are also shown in Figs. (d) and (e). White scale bars represent 1 μm in Fig. 2(c) and 200 nm in Figs. 2(d) and (e). We observed tetrahedral and hexagonal AlGaAs nanostructures, whose side-wall crystal facets tended to be rotated randomly, comparing to the case of the samples on the Si (111) substrates, as marked by white broken-lined triangles and hexagons in the Fig. 2(c). The height and diameter of these hexagonal nanostructures were smaller than 100 nm and 100 to 300 nm, respectively. Polycrystalline AlGaAs nanostructures were also observed, which was similar to the case of the samples on the Si (111) substrates.

For the structural characterizations of the samples observed in Fig. 2, next, we performed XRD measurements to clarify crystal orientations of the AlGaAs nanostructures. XRD spectra for both of the

samples had the marked peaks at $2\theta \approx 27.3^\circ$, and these were attributable to the diffractions from AlGaAs {111} planes, as shown Fig. 3. This result indicated that the growth of {111} planes was predominant even on an amorphous glass substrate, although the peak from AlGaAs {111} planes on the amorphous glass substrate was much weaker than that on the Si (111) substrate. There was no peak detected for crystalline Al₂O₃ layers.

Subsequently, we observed by TEM the differences of crystal structures of AlGaAs nanostructures and Al₂O₃ layers between on Si (111) and amorphous glass substrates. Figures 4(a) show cross-sectional TEM images using an electron-beam injection perpendicular to one of the side-wall crystal facets, i.e. {0-11}, of hexagonal AlGaAs nano-pillars or NWs grown on 5-nm-thick Al₂O₃ layers on Si (111) substrate. We observed that AlGaAs nanostructures were formed on Al₂O₃ layers, and that the $\langle 111 \rangle$ direction of hexagonal AlGaAs nano-pillars was parallel to the Si $\langle 111 \rangle$ direction, as shown in Fig. 4(a). Hexagonal AlGaAs nano-pillars had a zinc-blende-type crystal structure, judging from an electron-beam diffraction pattern (not shown here). Figures 4(d) shows cross-sectional TEM images using an electron-beam injection perpendicular to one of the side-wall crystal facet planes of hexagonal AlGaAs nano-pillars grown on 20-nm-thick Al₂O₃ layer on an amorphous glass substrate. The observed hexagonal AlGaAs nano-pillar structure was slightly tilted by approximately 7° against the substrate plane. Dark and bright thin layers observed on the AlGaAs nano-pillars were the Pt/Pd thin films for the SEM observations on the insulating glass substrate. We observed that the AlGaAs nano-pillar was formed on Al₂O₃ layers, and that the $\langle 111 \rangle_B$ direction was parallel to the vertical direction of hexagonal nano-pillar structure, as shown in the inset of Fig. 4(d). The black broken line in Fig. 4(d) represents the interface between the Al₂O₃ layers and the glass substrate, and the thickness of Al₂O₃ layers was approximately 18 nm, which were estimated from a typical TEM image. White or black scale bars represent 5 nm in Figs. 4(b), (c), (e), and (f). Figure 5 shows the highly-magnified TEM image of the crystallized γ -Al₂O₃ layers under the hexagonal AlGaAs nano-pillar observed in Fig. 4(d). We observed that crystal grains were formed near the layer surface, and that their size was roughly estimated to be about 20 nm at most. The black broken lines in the Al₂O₃ layers represent the roughly-drawn γ -Al₂O₃ grain boundaries in terms of the grains with different lattice orientations.

The structural characterization results by SEM, XRD, and TEM from Figs. 2 to 4 showed that hexagonal AlGaAs nano-pillars or NWs had a {111}B top surface. It has been reported that GaAs NWs fabricated by our SA-MOVPE have a {111}B top surface and six-fold {0-11} side-wall facets, as typically reported in Ref. [6]. Therefore, it is plausible that the observed AlGaAs nano-pillars, or NWs, grown on Al₂O₃ layers on Si (111) and amorphous glass substrates in the current work similarly have six-fold {0-11}-oriented crystal facets as a side-wall of the AlGaAs hexagonal prisms. In addition, for the structures observed in the samples on an amorphous glass substrate shown in Figs. 2(d) and (e), it is reasonable that tetrahedral AlGaAs nanostructures in Fig. 2(d) have the tilted {-1-10} top facets as a low Miller index, and that the hexagonal ones in Fig. 2(e) have the {111}B and tilted {-1-10} top facets, judging from our previous studies [10].

Bibliography

- [1] I. Levin and D. Brandon, *J. Am. Ceram. Soc.* **81**, 1995 (1998).
- [2] K. Wefers and C. Misra, Alcoa Technical Paper No. 19, Alcoa Laboratories, Pittsburgh, PA, 1987.
- [3] S. J. Wilson, "Phase Transformations and Development of Microstructure in Boehmite-Derived Transition Aluminas," *Proc. Br. Ceram. Soc.*, **28**, 281 (1979).
- [4] B. C. Lippens and J. H. De Boer, "Study of Phase Transformations during Calcination of Aluminum Hydroxides by Selected Area Electron Diffraction," *Acta Crystallogr.*, **17**, 1312 (1964).
- [5] S. Jakschik, U. Schroeder, T. Hecht, M. Gutsche, H. Seidl, and J. W. Bartha, *Thin Solid Films* **425** (2003) 216
- [6] L. Zhang, H. C. Jiang, C. Liu, J. W. Dong, and P. Chow, *J. Phys. D: Appl. Phys.* **40** (2007) 3707
- [7] C. M. Tanner, M. F. Toney, J. Lu, H. O. Blom, M. Sawkar-Mathur, M. A. Tafesse, and J. P. Chang, *J. Appl. Phys.* **102** (2007) 104112
- [8] W. E. Fenwick, N. Li, T. Xu, A. Melton, S. Wang, H. Yu, C. Summers, M. Jamil, and I. T. Ferguson, *J. Cryst. Growth* **311** (2009) 4306
- [9] N. Li, S. J. Wang, C. L. Huang, Z. C. Feng, A. Valencia, J. Nause, C. Summers, and I. Ferguson, *J. Cryst. Growth* **310** (2008) 4908
- [10] K. Ikejiri, F. Ishizaka, K. Tomioka, and T. Fukui, *Nanotechnology*, **24** (2013) 115304

Chapter 4 Growth of semiconducting nanowire on Al₂O₃/glass substrate

4.1 Introduction

Recently, the growth of NWs and nanopillars has been demonstrated on non-single-crystalline substrates, such as amorphous glass [1, 2], thermally-oxidized SiO₂ layers [3], and polycrystalline Si [4, 5]. In particular, amorphous glass is quite important and promising as a substrate for the realization of solar cells and light-emitting diodes on low-cost substrates as the eco-friendly green nanotechnologies because it is mostly much transparent, less toxic, much widely available, and cheaper than a conventional semiconducting substrate. However, the NWs directly grown on an amorphous glass substrate still have shown a relatively poor controllability of their sizes, positions, directions, and shapes owing to amorphous substrate materials. Therefore, a pre-orienting film or a metal catalyst on an amorphous substrate is required for the nucleation to enhance the NW growth in previous studies [1, 2].

We have been using thin amorphous Al₂O₃ layers deposited by atomic layer deposition (ALD) as interlayers on an amorphous glass substrate to help the nucleation before the growth of semiconductor alloy nanostructures and NWs. It has been reported that thin amorphous Al₂O₃ layers deposited by ALD are crystallized after the anneal treatment at a relatively high temperature [6 - 8]. Furthermore, the epitaxial growth of semiconductors on Al₂O₃ layers deposited on single-crystalline substrates by ALD has been

demonstrated, e.g., GaN growth on Si (111) substrate and InGaN growth on ZnO (0001) substrate with the Al₂O₃ interlayers [9, 10]. In this chapter, we demonstrate the growth of NWs and AlGaAs nanostructures on thin amorphous Al₂O₃ layers deposited by ALD on an amorphous glass substrate. For the preliminary characterization of crystal structures, we report on the results of hydrogen anneal treatment experiments for the crystallization in the planar amorphous Al₂O₃ layers and AlGaAs growth experiments on the crystallized Al₂O₃ interlayers on a planar amorphous glass substrate. We finally describe the experimental results of the NW formation on AlGaAs nanostructure buffers grown by utilizing the crystallization techniques of thin amorphous Al₂O₃ interlayers on an amorphous glass substrate.

4.2 Experimental procedures

NWs and AlGaAs nanostructure buffers were grown on Al₂O₃ layers deposited by ALD on an amorphous glass substrate, which was synthetic quartz, AQ series, manufactured by ASAHI GLASS Co. Ltd. We deposited thin amorphous Al₂O₃ layers by ALD on the amorphous glass substrate. We annealed the samples for crystallizing the amorphous Al₂O₃ layers in the reactor of metal-organic vapor phase epitaxy (MOVPE) set-up, and then, AlGaAs nanostructures were grown by MOVPE on the crystallized Al₂O₃ interlayers deposited on an amorphous glass substrate. After the growth of AlGaAs nanostructure buffers, finally, NWs were formed by the GaAs growth.

Al₂O₃ layers with the thickness of 5 to 20 nm were deposited at the temperature of 300 °C with (CH₃)₃Al and H₂O as the precursors in the ALD system. The temperature and time of anneal treatment in H₂ atmosphere in the MOVPE reactor for the crystallization experiments of the Al₂O₃ layers were 975 °C and 10 minutes, respectively. For the MOVPE growth of NWs and AlGaAs nanostructure buffers, (CH₃)₃Ga, (CH₃)₃Al, and 20%-AsH₃ diluted in H₂ were used as source materials. The estimated partial pressures of

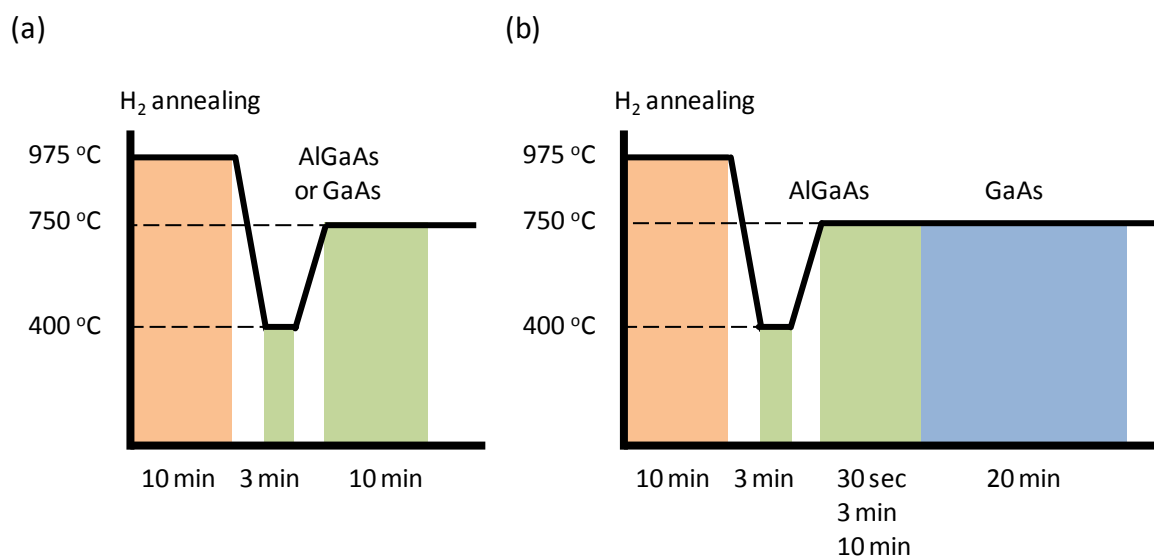


Fig. 4-1 Sequences for (a) the growth experiments of AlGaAs on Al₂O₃ interlayers deposited on amorphous glass substrates, and two reference experiments of (i) AlGaAs growth directly on amorphous glass substrates without any deposition of Al₂O₃ interlayers and (ii) GaAs growth directly on Al₂O₃ interlayers deposited on amorphous glass substrates without any AlGaAs nanostructure buffers, and for (b) the GaAs nanowire growth on AlGaAs nanostructure buffers grown on Al₂O₃ interlayers on amorphous glass substrates.

(CH₃)₃Ga, (CH₃)₃Al, and AsH₃ in the MOVPE reactor were approximately [(CH₃)₃Ga] = 2.0 × 10⁻⁶, [(CH₃)₃Al] = 3.3 × 10⁻⁷, and [AsH₃] = 1.2 × 10⁻³ atm, for the AlGaAs nanostructures, and [(CH₃)₃Ga] = 3.1 × 10⁻⁶ and [AsH₃] = 2.5 × 10⁻⁴ atm, for the NWs, respectively. Two types of the growth sequences are summarized in Fig. 1. Figure 4-1(a) shows the growth sequence mainly for the AlGaAs nanostructure growth experiments on the crystallized Al₂O₃ interlayers deposited on an amorphous glass substrate and their structural characterizations. After the anneal treatment at 975 °C for 10 minutes in H₂ atmosphere before the AlGaAs growth, only H₂ was introduced into the MOVPE reactor during the decrease in temperature to the growth temperature, T_g, for AlGaAs. AlGaAs was grown first at a relatively low T_g of 400 °C for 3 minutes as buffer layers possibly to enhance the AlGaAs nucleation on a substrate, and then at T_g of 750 °C for 10 minutes. Under these growth conditions for the AlGaAs nanostructures, we roughly estimated the volume of AlGaAs nanostructures (or nanodisks) grown on a reference substrate of bared single-crystalline Si (111) in the growth sequence shown in Fig. 4-1(a). We confirmed by surface and cross-sectional scanning electron microscope (SEM)

observations that the coverage ratio and the average height of AlGaAs nanodisks directly grown on the Si (111) substrate was about 87% and 60 nm, respectively. The growth sequence in Fig. 4-1(a) was also used for the reference experiments of (i) AlGaAs growth directly on an amorphous glass substrate without any deposition of Al₂O₃ interlayers and (ii) GaAs growth directly on 5-nm-thick Al₂O₃ interlayers deposited on an amorphous glass substrate without any AlGaAs nanostructure buffers. Figure 4-1(b) shows the growth sequence for the NWs on AlGaAs nanostructure buffers grown on 5-nm-thick Al₂O₃ interlayers deposited on an amorphous glass substrate. We only changed the growth time of AlGaAs nanostructure buffers from 30 seconds to 10 minutes before the GaAs growth to obtain the NWs.

SEM was used for the observation of AlGaAs nanostructure buffers, NWs, and surface morphologies, and transmission electron microscopy (TEM) was used for the structural characterizations in detail by the cross-sectional lattice image observations of AlGaAs nanostructures and Al₂O₃ layers. To observe the structures grown on an amorphous glass substrate by SEM, conductive Pt/Pd thin films were deposited by ion sputtering after the growth because a glass substrate is an insulator. We also used X-ray diffraction (XRD) for the structural characterizations of AlGaAs nanostructures.

4.3 Growth and structural characterization of AlGaAs on crystallized Al₂O₃ interlayers deposited on an amorphous glass substrate

We conducted the AlGaAs growth experiments in order to obtain the details about surface morphologies and crystal structures of AlGaAs and Al₂O₃ layers on amorphous glass substrates. First, we carried out the AlGaAs growth directly on an amorphous glass substrate, i.e., on a bared glass substrate without any Al₂O₃ interlayers. As shown in Fig. 4-2(a), the top view of SEM image revealed that no growth of marked AlGaAs nanostructures was observed. Subsequently, amorphous Al₂O₃ layers were introduced as interlayers between semiconducting layers and an amorphous glass substrate. After the anneal treatment in H₂ atmosphere before the growth by the sequence in Fig. 4-1(a), first, GaAs layers were grown on 5-nm-thick planar Al₂O₃ layers. Figure 4-2(b) shows a typical top view of SEM image, in which we have observed almost no growth of GaAs on the Al₂O₃ layers. White scale bars represent 1 μm in Figs. 4-2(a) and (b). Next, we conducted the growth experiments of AlGaAs nanostructures on 5-nm-thick planar Al₂O₃ layers deposited on an amorphous glass substrate. Figure 4-2(c) shows a typical SEM top view of AlGaAs nanostructures, and highly-magnified SEM bird's-eye views of AlGaAs nanostructures are shown in Figs. 4-2(d) and (e). White scale bars represent 1 μm in Fig. 4-2(c) and 200 nm in Figs. 4-2(d) and (e). We observed tetrahedral and hexagonal AlGaAs nanostructures, whose side-wall crystal facets tended to be rotated randomly, as marked by white broken-lined triangles and hexagons in the Fig. 4-2(c). The height and diameter of the hexagonal nanostructures were smaller than 100 nm and 100 to 300 nm, respectively. Polycrystalline AlGaAs nanostructures were also observed. The purpose of the low-temperature-grown AlGaAs buffer layers at T_g of 400 °C for 3 minutes is to enhance the AlGaAs nucleation on a substrate. In the reference AlGaAs growth experiments at T_g of 750 °C for 10 minutes on 5-nm-thick Al₂O₃ layers deposited on a Si (111) substrate, we observed that the coverage ratio of AlGaAs nanostructures on the 5-nm-thick Al₂O₃ layers was

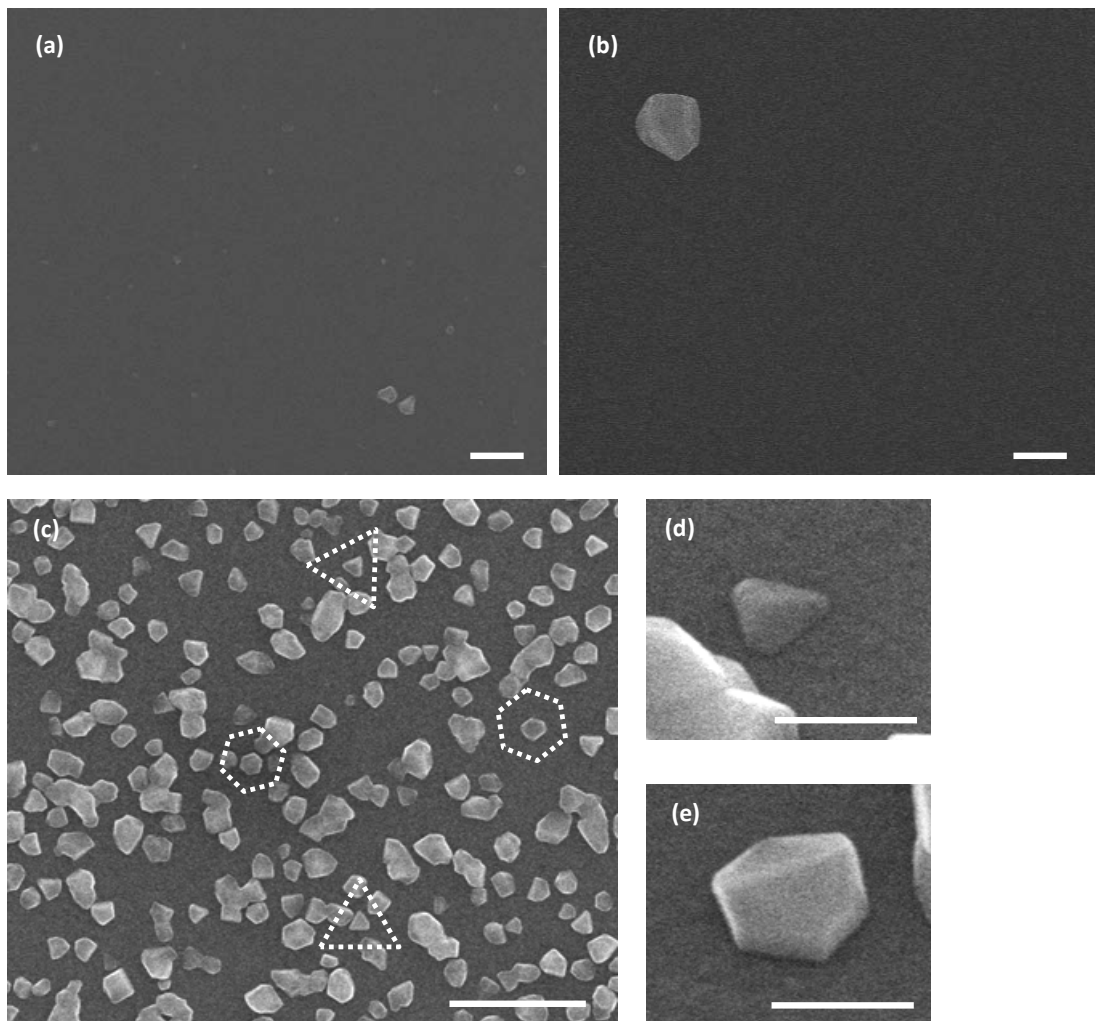


Fig. 4-2 Top views of SEM images for the samples after (a) the AlGaAs growth directly on an amorphous glass substrate and (b) the GaAs growth on 5-nm-thick Al₂O₃ layers deposited on an amorphous glass substrate. AlGaAs nanostructures on 5-nm-thick Al₂O₃ layers deposited on an amorphous glass substrate: (c) is the top view of SEM image, and (d) and (e) are the bird's-eye views of highly-magnified SEM images for typical structures with a tetrahedral and hexagonal shape, respectively. White scale bars represent 1 μm in (a), (b), and (c), and 200 nm in (d) and (e), respectively.

much higher, and that the size of them was much smaller by introducing the low-temperature-grown AlGaAs buffer layers than without introducing them in the current work. It has been reported that low-temperature-grown buffer layers are effective to enhance the nucleation at the initial stages of the thin film growth in the lattice mismatched materials system [31 - 33]. Therefore, it was highly possible that the AlGaAs nanostructures observed in Fig. 4-2(c) were formed during the AlGaAs growth at T_g of 400 °C for 3 minutes in

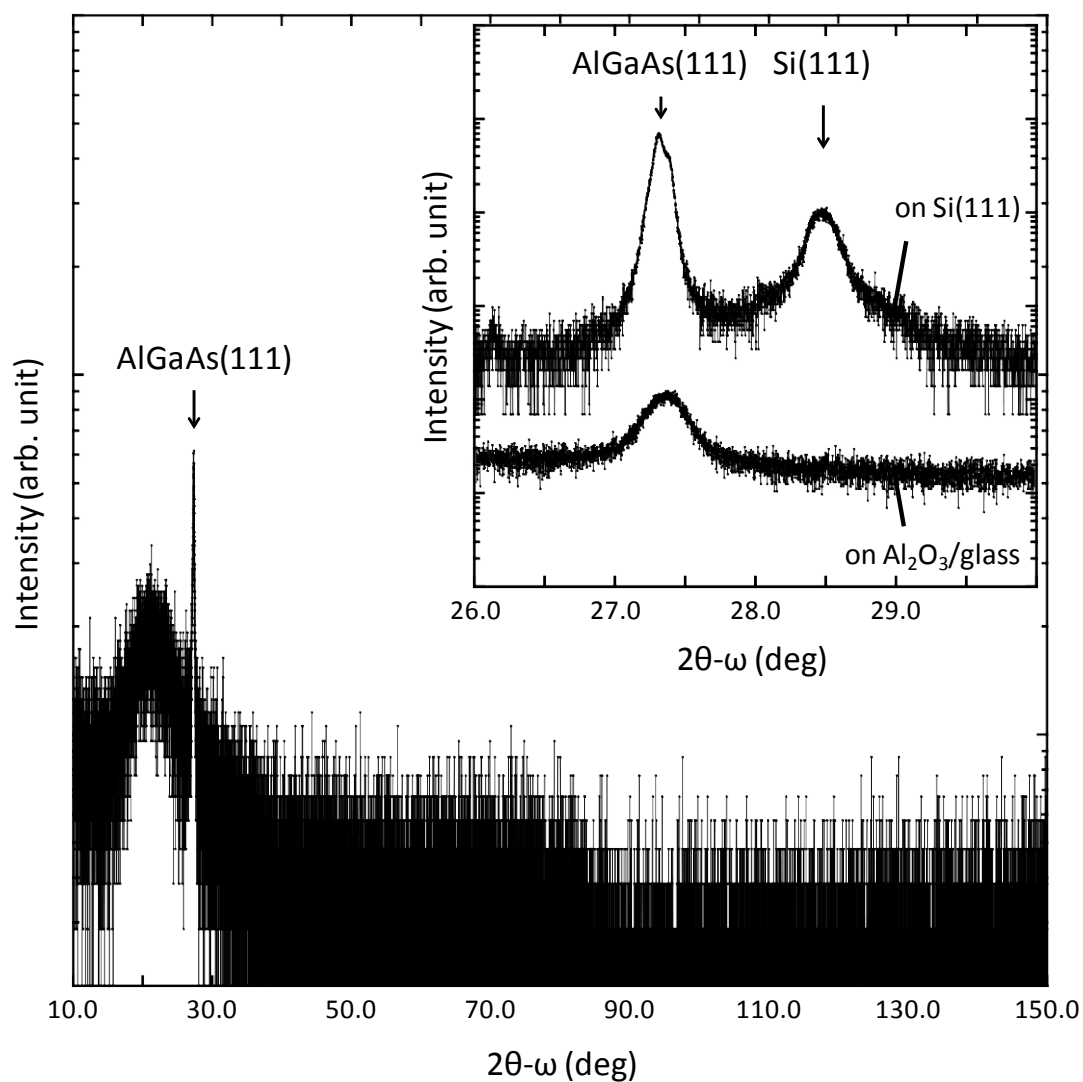


Fig. 4-3 XRD rocking curve in logarithmic scale for the sample on an amorphous glass substrate observed in Fig. 2. The inset represents the highly-magnified rocking curve detected from $2\theta = 26^\circ$ to 30° . The rocking curve for the sample on a Si (111) substrate is also shown in the inset as a reference to compare the differences between the amorphous and single-crystalline substrates.

the growth sequence in Fig. 4-1(a). It was effective to introduce the low-temperature-grown AlGaAs buffer layers for enhancing the growth of high-density AlGaAs nanostructures in the current work.

For the structural characterizations of the samples observed in Fig. 4-2, next, we performed XRD measurements in Fig. 4-3 to clarify crystal orientations of the AlGaAs nanostructures. A Si (111) substrate

was also used as a reference to compare the differences between the amorphous and single-crystalline substrates. XRD spectra for both of the samples had the marked peaks at $2\theta \approx 27.3^\circ$, and these were attributable to the diffractions from AlGaAs {111} planes, as shown in the inset of Fig. 4-3. There was no other marked peak detected for AlGaAs layers with different crystal orientations, i.e., the diffractions from {004}, {022}, and so on, except for a broad and weak background spectrum ranged from $2\theta =$ around 15° to 30° , in the wide range XRD measurement from $2\theta = 10^\circ$ to 150° , although we observed that large numbers of polycrystalline AlGaAs nanostructures were grown as well as tetrahedral and hexagonal AlGaAs nanostructures. This result indicated that the growth of {111} planes seemed to be predominant even on an amorphous glass substrate, although the peak from AlGaAs {111} planes on the amorphous glass substrate was much weaker than that on the Si (111) substrate. There was no peak detected for crystalline Al₂O₃ layers. Subsequently, we observed by TEM the crystal structures of AlGaAs nanostructures and Al₂O₃ layers on an amorphous glass substrate. Figures 4-4(a) to (c) show cross-sectional TEM images using an electron-beam injection perpendicular to one of the side-wall crystal facet planes of hexagonal AlGaAs nanodisks grown on 20-nm-thick planar Al₂O₃ layers on an amorphous glass substrate. As shown in Fig. 4-4(a), the observed hexagonal AlGaAs nanodisk structure was slightly tilted by approximately 7° against the substrate plane. Dark and bright thin layers observed on the AlGaAs nanodisks were the Pt/Pd thin films for the SEM observations on the insulating glass substrate. We observed that the hexagonal AlGaAs nanodisk was formed on Al₂O₃ layers, and that the $\langle 111 \rangle_A$ or B direction was parallel to the vertical direction of the hexagonal nanodisk structure, as shown in the inset of Fig. 4-4(a). The black broken-line in Fig. 4-4(a) represents the estimated interface between the Al₂O₃ layers and the glass substrate, and the thickness of Al₂O₃ layers was approximately 18 nm, which were estimated from a typical TEM image. From high-resolution TEM observations for the Al₂O₃ layers, as shown in Figs. 4-4(b) and (c), lattice fringes of γ -Al₂O₃ {111} planes were observed. Black scale bars represent 5 nm in Figs. 4-4(b) and (c). It was estimated by the fast Fourier transform, or FFT, from the observed lattice images that these lattice fringes were attributable to the lattice spacing of 0.46 nm, and that it was in good agreement with the well-known literature value of 0.456 nm for the

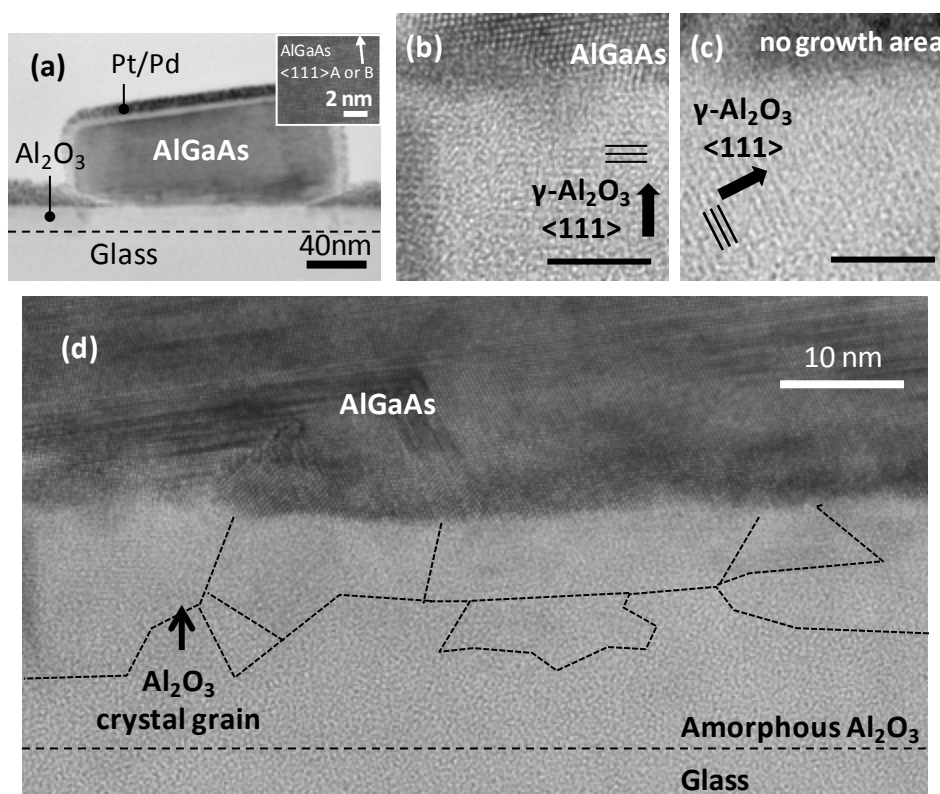


Fig. 4-4 Cross-sectional TEM images: (a) for a typical hexagonal AlGaAs nanostructure, (b) for lattice images of Al₂O₃ layers under the hexagonal AlGaAs nanostructures of (a), (c) for lattice images of Al₂O₃ layers in no AlGaAs growth area on the Al₂O₃ layers. (a) to (c) are on 20-nm-thick Al₂O₃ layers on an amorphous glass substrate. The insets of (a) shows a lattice image of AlGaAs nanostructures. Black scale bars in (b) and (c) represent 5 nm. Electron-beam injection was perpendicular to one of the side-wall planes of AlGaAs hexagonal prisms. (d) Cross-sectional TEM lattice image around the interface between AlGaAs and Al₂O₃. Thickness of the Al₂O₃ layers was estimated to be about 18 nm under the hexagonal AlGaAs nanostructure in (d). Black broken lines represent roughly-drawn boundaries between γ -Al₂O₃ crystal grains.

{111} planes of γ -Al₂O₃ (from the JCPDS database). Some of the γ -Al₂O₃ {111} planes were parallel to the glass substrate surface, whereas others were tilted against the substrate. Therefore, we concluded that the crystallized γ -Al₂O₃ layers were a polycrystalline. Figure 4-4(d) shows the highly-magnified TEM image of the crystallized γ -Al₂O₃ layers under the hexagonal AlGaAs nanodisk observed in Fig. 4-4(a). We observed that crystal grains were formed near the layer surface, and that their size was roughly estimated to be about 20 nm at most. The black broken-lines in the Al₂O₃ layers represent the roughly-drawn γ -Al₂O₃ grain

boundaries in terms of the grains with different lattice orientations. From some of the cross-sectional TEM observation results around the Al₂O₃ layer surfaces including Fig. 4-4(d), we observed that the surface roughness on the Al₂O₃ layers was 2.3 nm at maximum. This roughness was observed on the Al₂O₃ layers in the areas both with and without a AlGaAs nanostructure on the Al₂O₃ layers. As reported in Ref. [27], some researchers observed that the Al₂O₃ layer surfaces became rough possibly in the crystallization process of amorphous Al₂O₃ layers during the high temperature annealing. Therefore, it was likely in the current work that the surface roughness of 2.3 nm was caused on the Al₂O₃ layers during the anneal treatment at 975 °C for 10 minutes in H₂ atmosphere before the AlGaAs growth, although further experiments are required to conclude.

The structural characterization results by SEM, XRD, and TEM from Figs. 4-2 to 4-4 showed that hexagonal AlGaAs nanostructures or nanodisks had a {111}A or B top surface. It has been reported that GaAs NWs fabricated by our SA-MOVPE have a {111}B top surface and six-fold {0-11} side-wall facets, as typically reported in Ref. [13]. The AlGaAs nanostructures in the current work are the different case from the NWs grown by SA-MOVPE. However, it might be plausible that the observed AlGaAs nanodisks grown on Al₂O₃ layers on amorphous glass substrates in the current work similarly have six-fold {0-11}-oriented crystal facets as a side-wall of the AlGaAs hexagonal prisms. In addition, for the structures observed in the samples on an amorphous glass substrate shown in Figs. 4-2(d) and (e), although further structural characterizations are required to conclude, it might be possible that tetrahedral AlGaAs nanostructures in Fig. 4-2(d) have the tilted {-1-10} top facets as a low Miller index, and that the hexagonal ones in Fig. 4-2(e) have the {111}B and tilted {-1-10} top facets, judging from the tetrahedral and hexagonal shape of the observed AlGaAs nanostructures, the TEM observations of the hexagonal AlGaAs nanodisks in Fig. 4-4, and our previous studies [13]. We observed that there was a slight discrepancy between the XRD peak position of $2\theta \approx 27.3^\circ$, which was attributable to the diffraction from AlGaAs {111} planes, in Fig. 4-3, and the TEM image in Fig. 4-4(a), since the observed hexagonal AlGaAs nanodisk structure in Fig. 4-4(a) was slightly tilted by approximately 7° against the substrate plane. To clarify the reasons for this discrepancy, further experiments

are required. However, it might appear that most of the hexagonal AlGaAs nanostructures grown over the Al₂O₃ layer surfaces were possibly oriented in an approximately “vertical” direction, since we have observed in the top views of SEM images that most of the observed hexagonal AlGaAs nanostructures seems to be nearly “vertical”. It is well known that the bulk Al₂O₃ shows its stability in some of the crystal structures, i.e., α , γ , θ , and κ phases [34]. Theoretical model of crystallization kinetics for a thin amorphous film has been also investigated [35]. Therefore, it is possible that the γ -phase Al₂O₃ crystal grains have been formed as a stable phase in amorphous Al₂O₃ layers in the current work. In the case of the samples on single-crystalline substrates, such as Si (111) and 4H-SiC (0001), it was reported that amorphous Al₂O₃ layers were crystallized with the epitaxial relationship with the substrate materials [27, 28]. But, in the case of the samples on an amorphous glass substrate here, some of the γ -Al₂O₃ crystal grains with tilted crystal axes were formed presumably because there is no epitaxial relationship between the crystallization in amorphous Al₂O₃ layers and an amorphous glass substrate.

4.4 Dependence of AlGaAs growth on Al₂O₃ layer thickness on an amorphous glass substrate

Next, from the results discussed in the previous subsection, we conducted the growth experiments of AlGaAs layers on the crystallized Al₂O₃ interlayers with a different thickness on an amorphous glass substrate in order to evaluate the optimum thickness of Al₂O₃ layers for the crystallized γ -Al₂O₃ interlayers and the AlGaAs nanostructure growth on them. AlGaAs layers were grown on the ALD-deposited Al₂O₃ layers with the thickness of 5, 10, and 20 nm on an amorphous glass substrate. Figure 4-5(a) shows a summary of the AlGaAs coverage ratios (%) as a function of the thickness of deposited Al₂O₃ layers. The three types of morphologies on the grown samples, i.e., “hexagonal prism”, “polycrystal”, and “no growth”, were defined to

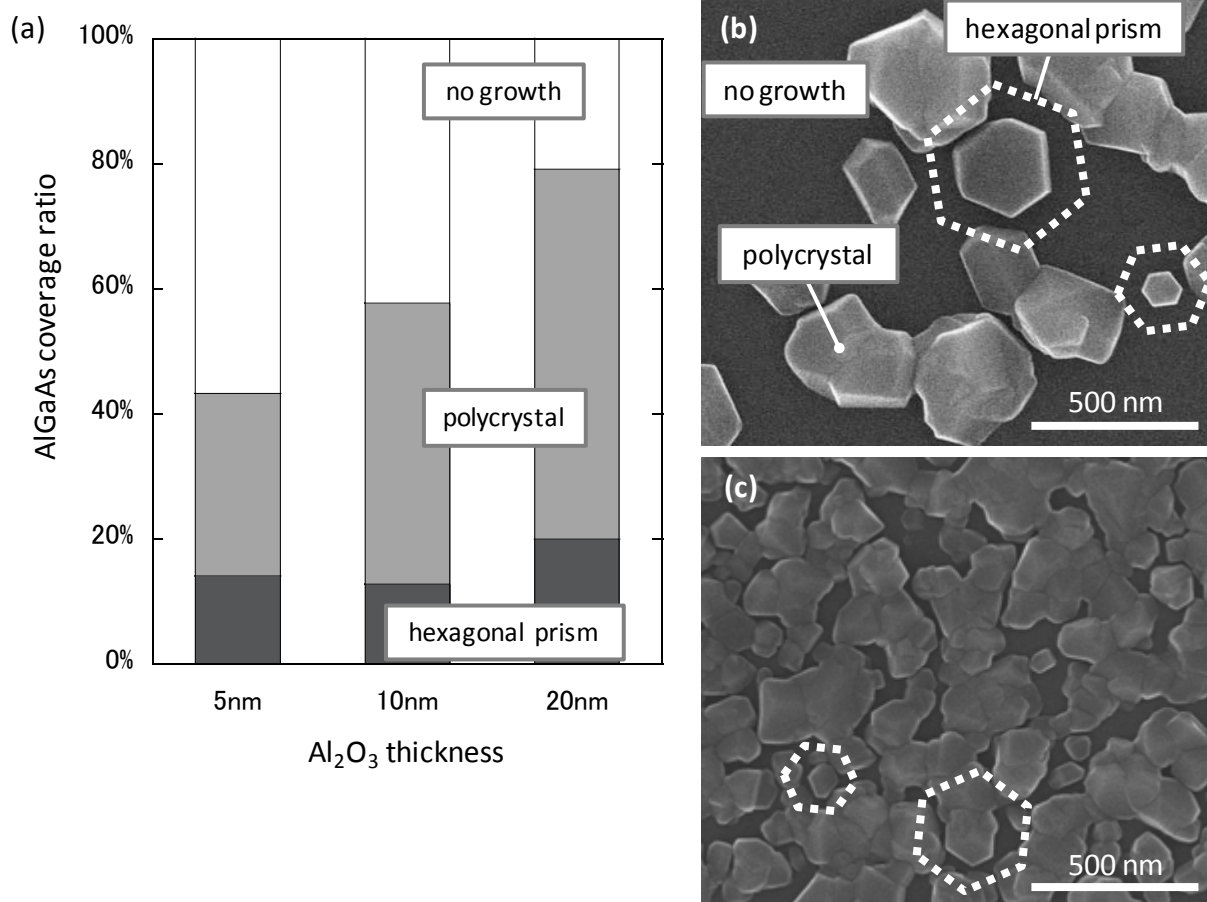


Fig. 4-5 (a) Coverage ratios for the three types of morphologies on the grown samples, i.e., “hexagonal prism”, “polycrystal”, and “no growth”, as a function of the thickness of Al₂O₃ layers. Typical top view of highly-magnified SEM image for AlGaAs nanostructures grown on (b) 5- and (c) 20-nm-thick Al₂O₃ layers on an amorphous glass substrate.

estimate the coverage ratios. Figures 4-5(b) and (c) show typical top views of SEM images for the samples with the ALD-deposited 5- and 20-nm-thick Al₂O₃ layers, respectively. The appearance ratio for the hexagonal prism was nearly independent of the thickness of Al₂O₃ layers. On the other hand, the appearance ratio for all of the AlGaAs-grown areas including the hexagonal prisms increased with increasing the thickness of Al₂O₃ layers. The ratio of the hexagonal prisms to all the AlGaAs-grown areas including the polycrystals was estimated to be approximately 30% in the case of the samples on 5-nm-thick Al₂O₃ layers. The coverage ratio and the average height of AlGaAs nanostructures, including hexagonal nanodisks and polycrystals, on 20-nm-thick Al₂O₃ layers were estimated to be 79% and 65 nm, respectively, from a typical cross-sectional

low-magnification TEM image. Therefore, we concluded that the volume of AlGaAs nanostructures grown on the 20-nm-thick Al₂O₃ layers had no significant difference from that on the reference substrate of bared single-crystalline Si (111), i.e., the coverage ratio of 87% and the average height of 60 nm, as estimated in Section 2. In some of the polycrystalline AlGaAs nanostructures observed in a typical cross-sectional TEM image, we observed that there were several types of the crystal grains formed possibly along a different “titled” crystal axis as well as the $\langle 111 \rangle$ A or B axis, judging from the lattice fringes observed in the lattice images. As estimated from Fig. 4-5(b), approximately 30% of the observed three types of morphologies on the grown samples were “polycrystal”. Therefore, the XRD spectrum from the AlGaAs nanostructures grown on the 5-nm-thick Al₂O₃ layers on the glass substrate in Fig. 4-3 possibly indicated that it was too weak to be detected for the diffractions from the AlGaAs polycrystals with a different crystal axis tilted in a various direction.

From the experimental results shown in Fig. 4-5, the possible growth mechanisms are discussed. Figure 4-6 depicts the schematic illustrations for the samples with thinner and thicker Al₂O₃ layers deposited on an amorphous glass substrate. It was reported that there was a nearly linear relationship between the film thickness of the Al₂O₃ layers and the crystal grain size in the Al₂O₃ layers deposited by ALD [26, 28].

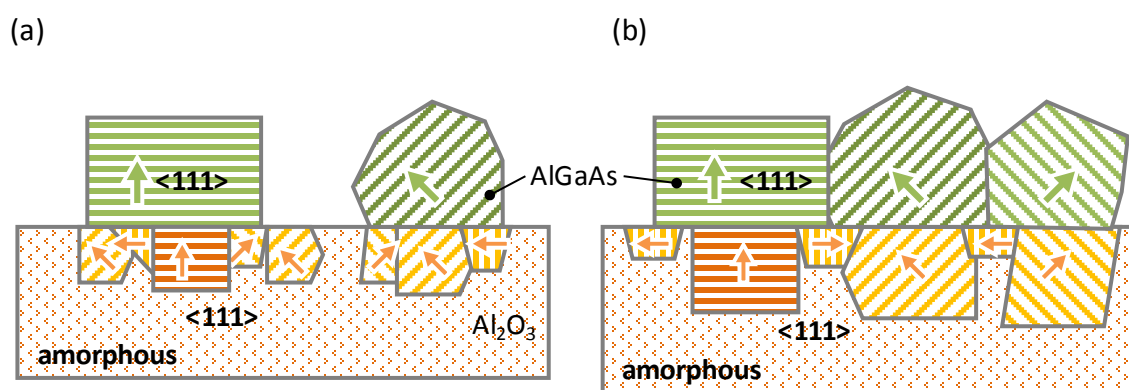


Fig. 4-6 Schematic illustrations for the possible explanation of the differences in the formation of AlGaAs nanostructures depending on the size of crystal grains of Al₂O₃: the cases of (a) thin and (b) thick Al₂O₃ layers.

Therefore, large crystal grains tended to be formed in the thicker Al₂O₃ layers. The size of γ -Al₂O₃ crystal grains in 20-nm-thick Al₂O₃ layers roughly estimated from the cross-sectional TEM image in Fig. 4-4(d) was approximately 20 nm at most in the current study. Although we have not observed thinner Al₂O₃ layers, e.g., 5 nm thick, by cross-sectional TEM, it is likely that the average size of γ -Al₂O₃ crystal grains is smaller in the 5-nm-thick Al₂O₃ layers than in the 20-nm-thick ones. In the case of the samples with the thicker Al₂O₃ layers, relatively large γ -Al₂O₃ crystal grains are formed in a wide area. Then, the nucleation of AlGaAs easily occurs on large γ -Al₂O₃ crystal grains, as illustrated in Fig. 4-6(b). After the nucleation of AlGaAs on the γ -Al₂O₃ crystal grains, AlGaAs nuclei in the neighborhood are merged together (Fig. 4-5(c)). In the case of the samples with the thinner Al₂O₃ layers with relatively small γ -Al₂O₃ crystal grains, on the other hand, it might be difficult that the nucleation of AlGaAs occurs on the small crystal grains. As a result, the nucleation density of AlGaAs becomes possibly lower, which leads to the increase in the no-growth area (Fig. 4-5(b)). These results seem to be consistent with the results of GaAs NW growth on polycrystalline Si by SA-MOVPE [24]. The appearance probability of the AlGaAs hexagonal prisms, whose $\langle 111 \rangle_A$ or B direction oriented nearly perpendicular to the substrate surface, was almost independent of the thickness of Al₂O₃ layers (Fig. 4-5(a)) possibly because there were also a large number of large titled γ -Al₂O₃ crystal grains which led to the AlGaAs polycrystals. In addition, since Al-O chemical bonds on the Al₂O₃ layer surface is quite stable, surface treatments of γ -Al₂O₃ layers might be very important to help the nucleation of AlGaAs on γ -Al₂O₃ crystal grains. In the case of GaN or AlN growth on single crystal α -Al₂O₃ substrates, the nitridation of the α -Al₂O₃ surfaces has been intensively demonstrated at a relatively low temperature of 200 °C or high temperature of 1,550 °C before the growth [36, 37]. Therefore, it might be effective for enhancing the nucleation of AlGaAs on γ -Al₂O₃ crystal grains to carry out the anneal treatment in 20%-AsH₃ with H₂ in the MOVPE reactor.

4.5 Selective-area growth of AlGaAs nanostructures on Al₂O₃/Si(111) substrate

We conducted selective-area growth of AlGaAs nanostructures on Al₂O₃ layers deposited on Si(111) substrate in order to come to realization of semiconducting nanowire fabricated on glass substrate.

For the growth experiments, after the deposition of Al₂O₃ layers by ALD and a 20-nm-thick SiO₂ mask by plasma-enhanced chemical vapor deposition, the initial SiO₂ mask openings were formed using electron beam lithography and reactive ion etching. Before the growth of the nanostructures, Si (111) substrates with Al₂O₃ and SiO₂ layers on top were annealed in H₂ atmosphere in our MOVPE reactor. Finally, AlGaAs nanostructures were grown by MOVPE on the Al₂O₃ layer surfaces in the initial mask openings of the SiO₂ layers.

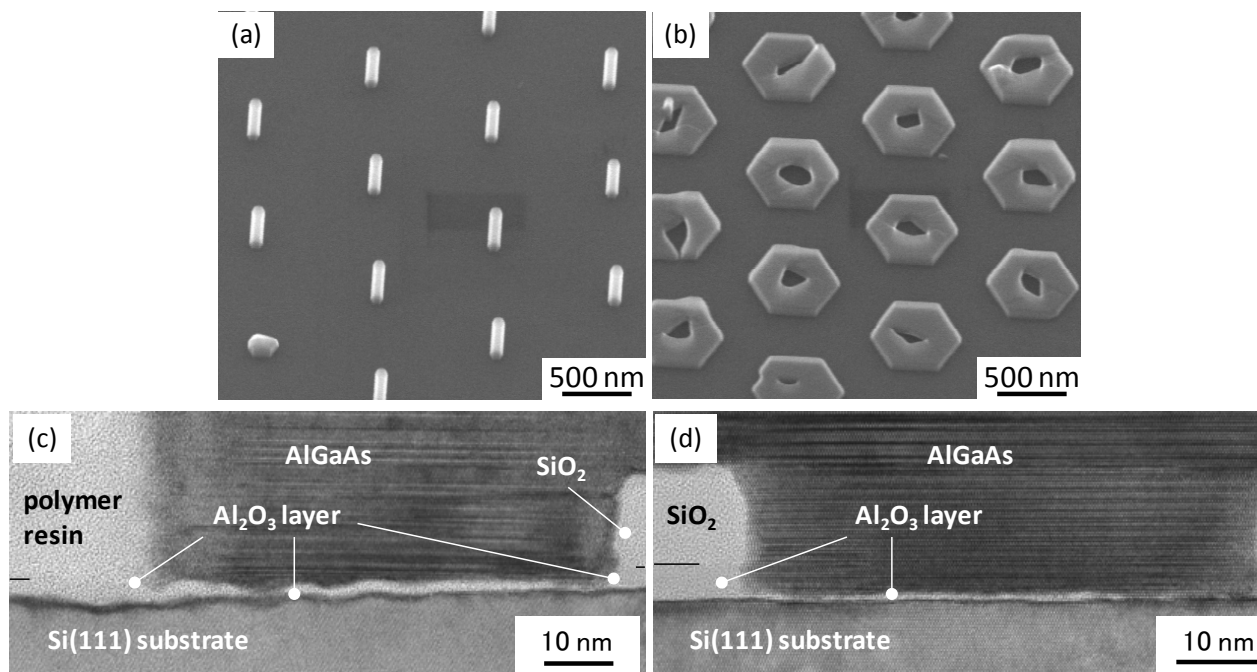


Fig. 4-7 45°-tilted SEM images of AlGaAs nanostructures on 5-nm-thick Al₂O₃ layers. Initial mask opening diameters are (a) 50 and (b) 500 nm, respectively. Cross-sectional TEM image and lattice image around the interface (c) of Fig. 4-7(a) and (d) of Fig. 4-7(d).

Figure 4-7 shows typical SEM images of AlGaAs nanostructures on the 5-nm-thick Al₂O₃ layers in the initial mask openings, whose diameters are 50 or 500 nm. The annealing in H₂ atmosphere was carried out for this sample at a temperature of 875 °C for 15 min. NWs and ring-shaped structures were confirmed at the initial mask openings with the diameter of 50 and 500 nm, respectively. Figure 4-7 are the cross-sectional TEM observation results for the AlGaAs nanostructure samples shown in the SEM image of Figs. 4-7(a) and 4-7(b), respectively. The cross-sectional images were taken for the areas nearly in the middle of the nanostructures from the <0-11> direction. We observed the thin layers with a bright contrast between AlGaAs layers and Si (111) substrates in the initial SiO₂ mask openings. The thin layers are supposed to be insulating Al₂O₃ layers, and the thickness of the layers was typically estimated to be 3 to 8 monolayers (MLs). We observed that the 3-ML-thick Al₂O₃ layers under the AlGaAs layers were possibly single crystalline, as shown in Fig. 4-7(c), and that thicker Al₂O₃ layers were partially crystallized. On the other hand, we confirmed that the Al₂O₃ layers between the SiO₂ mask layers and the Si (111) substrates were amorphous, and the thickness was about 4.5 nm. We estimated that approximately 4-nm-thick Al₂O₃ layers were etched off during the reactive ion etching process. AlGaAs nanostructures have been grown on the crystallized Al₂O₃ layers, but there is still a possibility that AlGaAs is grown from the pin-holes in the Al₂O₃ layers, where the Si (111) surface is unintentionally exposed, i.e. not covered by Al₂O₃.

In order to optimize the etching condition, we investigate the etching rate of Al₂O₃ layers. We prepared the 2 kinds of samples: Al₂O₃ layers without annealing, and annealed at 1000 °C for 3 min. In order to compare 2 kinds of etching process, we used RIE etching and buffered HF (BHF) etching under typical etching condition to form the SiO₂ mask openings. Etching selectivity between SiO₂ and Al₂O₃ are summarized in Table 4-1. We confirmed that annealed Al₂O₃ layer was not etched by BHF. Therefore, we conclude that BHF etching is useful for preparing the mask openings for selective-area growth on crystallized Al₂O₃ layers.

Conditions	selectivity
RIE/without annealing	4
RIE/annealed	4
BHF/without annealing	0.75
BHF/annealed	-

Table 4-1. Etching selectivity between SiO₂ and Al₂O₃.

4.6 Selective-area growth of AlGaAs nanostructures on amorphous glass substrate with crystallized Al₂O₃ interlayers

Figure 4-8 shows the top view of SEM image for the selective-area growth of AlGaAs nanostructures

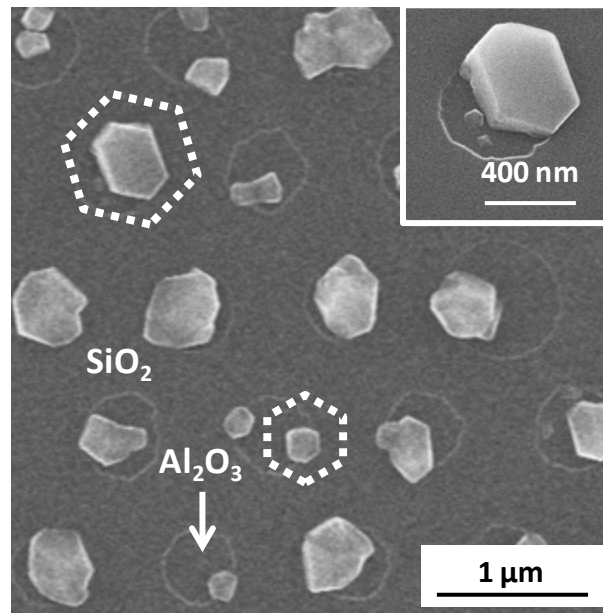


Fig. 4-8 Typical top view of SEM image of AlGaAs nanostructures selectively grown in the SiO₂-mask openings with the diameter of 400 nm on 20-nm-thick Al₂O₃ layers by SA-MOVPE. The inset shows the highly-magnified bird's-eye view of hexagonal AlGaAs nanostructure formed in the SiO₂-mask opening.

in the SiO₂-mask openings with the diameter of 400 nm on the 20-nm-thick Al₂O₃ layers deposited on an amorphous glass substrate. The inset in the figure shows the highly-magnified bird's-eye view of a typical hexagonal AlGaAs nanostructure grown in the SiO₂-mask openings. As shown in Fig. 48, AlGaAs nanostructures were grown only on the Al₂O₃ layer surfaces in the SiO₂-mask openings, and some of the nanostructures, as marked by white broken-lined hexagons in the figure, had a hexagonal nano-pillar shape, as similarly observed on the planar crystallized γ -Al₂O₃ layers shown in Fig. 4-2(c). On a bared amorphous glass substrate, i.e. no deposition of Al₂O₃ layers on it, which were introduced in the MOVPE reactor as a reference in the same growth run, we observed that only a small number of nanoparticles, which were possibly AlGaAs polycrystals, with a much smaller size were formed (not shown here). Therefore, these experimental results possibly showed that the observed AlGaAs nanostructures were epitaxially grown only on the crystallized γ -Al₂O₃ layers, whereas they were never formed on SiO₂-mask layers nor the bared glass surfaces.

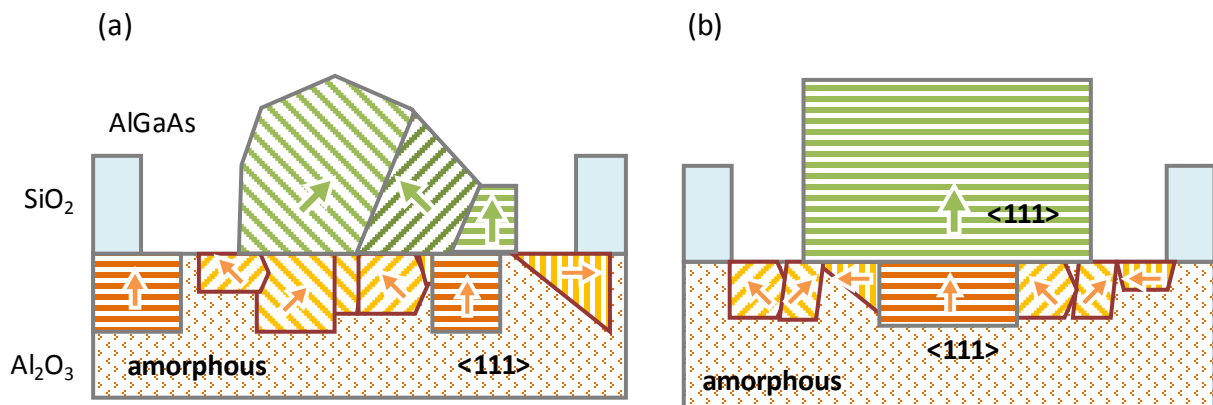


Fig. 4-9 Schematic illustrations to explain a possible formation mechanism for AlGaAs nanostructures in SiO₂-mask openings: (a) polycrystalline AlGaAs nanostructures caused by the nucleation from several Al₂O₃ crystal grains, and (b) hexagonal AlGaAs nano-pillars caused by the nucleation mainly from <111>-oriented Al₂O₃ crystal grains.

The γ -Al₂O₃ crystal grain size in the 20-nm-thick Al₂O₃ layers was roughly estimated to be about 20 nm at most from the cross-sectional TEM images in Fig. 4-4(d). It was much smaller than the diameter of

SiO₂-mask openings of 400 nm in the selective-area growth. Therefore, a large number of the γ -Al₂O₃ crystal grains presumably exist in the areas in the SiO₂-mask openings, as shown in the schematic illustrations in Fig. 4-9. The nucleation of AlGaAs possibly occurs on each of the γ -Al₂O₃ crystal grain surfaces in the SiO₂-mask openings. When an AlGaAs nucleus grows from different crystal grains in the same SiO₂-mask openings, some of the AlGaAs nuclei merge together, which leads to the formation of AlGaAs polycrystals. In contrast, hexagonal AlGaAs nano-pillars are formed possibly when the nucleation and the growth of AlGaAs on γ -Al₂O₃ {111} crystal grain surfaces are predominant, as illustrated in Fig. 4-9(b). Therefore, if we prepare the initial SiO₂-mask openings with a diameter of several tens nanometers, only one or two γ -Al₂O₃ crystal grains will exist in an area in a SiO₂-mask opening. That possibly makes us expect that an AlGaAs nanostructure grown in one SiO₂-mask opening is a single crystal. Therefore, we believe that our findings in the current work give important guidelines for the realization of vertical free-standing hexagonal NWs with a relatively small diameter of several tens nanometers [29] even on an amorphous glass substrate using our techniques in future.

4.7 Growth of nanowires on an amorphous glass substrate with AlGaAs nanostructure buffers on crystallized Al₂O₃ interlayers

By the GaAs growth using the crystallization technique of Al₂O₃ interlayers and AlGaAs nanostructure buffer technique, we demonstrated the NW formation on an amorphous glass substrate. The growth sequence for these growth experiments is summarized in Fig. 4-1(b). We only changed the growth time of AlGaAs nanostructure buffers from 30 seconds to 10 minutes before the GaAs growth on amorphous glass substrates with the same Al₂O₃ interlayer thickness of 5 nm. For the purpose of zinc-blende-type GaAs

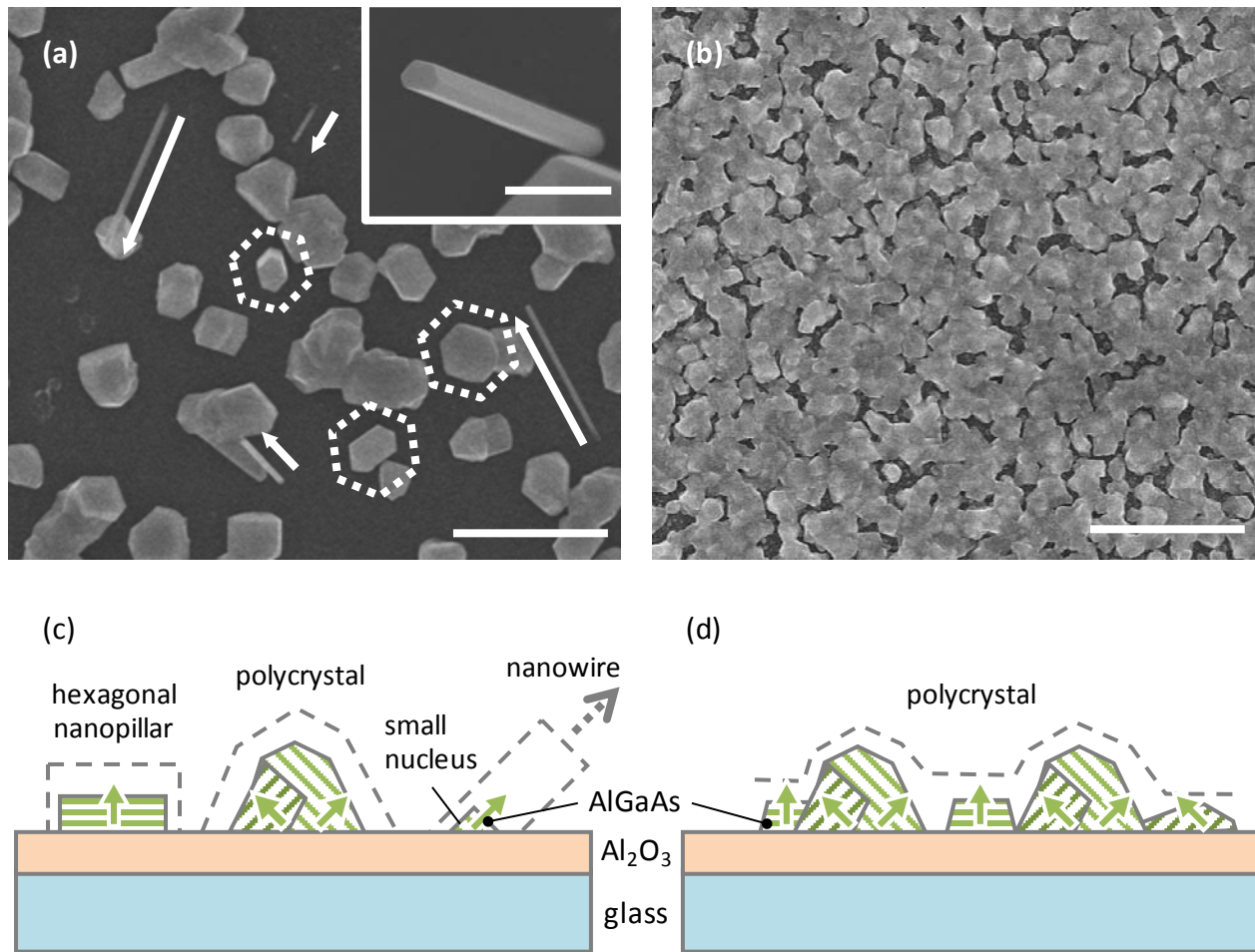


Fig. 4-10 Top views of SEM images of GaAs nanowires on AlGaAs nanostructure buffers. Only the growth time for the AlGaAs nanostructure buffers was changed: (a) 30 seconds and (b) 10 minutes. (c) and (d): Schematic illustrations for the possible explanation of the differences in the GaAs nanowire formation on AlGaAs nanostructure buffers, depending on the coverage with the AlGaAs buffers before the GaAs nanowire growth. White scale bars represent 4 μ m in (a) and (b), and 500 nm in the inset of (a), respectively.

NW growth on the AlGaAs nanostructure buffers, we chose our typical SA-MOVPE growth conditions to enhance the NW growth in the $\langle 111 \rangle_B$ direction [15]. Figures 4-10(a) and (b) show typical top views of SEM images after the GaAs growth on the AlGaAs nanostructure buffers. The AlGaAs nanostructure buffers were grown for 30 seconds and 10 minutes, respectively, before the GaAs growth. White scale bars represent 4 μ m in Figs. 4-10(a) and (b), and 500 nm in the inset of Fig. 4-9(a), respectively. We observed that the tilted NWs with a typical length of about 1 to 4 μ m or longer and diameter of about 140 to 180 nm were grown (as

marked by white thick arrows in Fig. 4-10(a)), in addition to the hexagonal nanopillars (as marked by white broken-lined hexagons in Fig. 4-10(a)). Detailed SEM observations revealed that the NWs were formed in the direction marked by white thick arrows in Fig. 4-10(a) from the substrate surfaces (not from the observed large AlGaAs polycrystals). As observed in the inset of Fig. 4-10(a), the NWs had a hexagonal prism shape, similarly in the case of the NWs grown by SA-MOVPE, which has shown that the NWs surrounded with six {0-11} side-wall facets are grown in the <111>B direction of a zinc-blende-type crystal structure [12 - 20]. With increasing the growth time of AlGaAs nanostructure buffers, the length of NWs decreased, and the tilted NWs on the AlGaAs nanostructure buffers grown for 3 minutes had a typical length of about 100 to 300 nm or longer and diameter of about 140 nm (not shown here). There was almost no change in the NW diameters, which might indicate that the NWs in the current work were grown in the <111>B direction similarly in the case of the NWs grown by SA-MOVPE in our previous studies [12 - 20]. Finally, we observed that no growth of the NWs occurred on the sample with the AlGaAs nanostructure buffers grown for 10 minutes, as shown in Fig. 4-10(b). As observed in Figs. 4-2(c) to (e), some of the AlGaAs nanostructures, which had a smaller diameter than the observed large AlGaAs polycrystals, had hexagonal prism and tetrahedral shapes with well-defined crystal facets. We observed almost no GaAs growth directly on the Al₂O₃ layers without the AlGaAs nanostructure buffers, as shown in Fig. 4-2(b). In addition, it was revealed that no GaAs growth occurred directly on the Al₂O₃ layers even under our typical SA-MOVPE growth conditions to enhance the GaAs NW growth in the <111>B direction (not shown here). Therefore, it might be possible that hexagonal “GaAs” NWs with well-defined crystal facets were grown on the tilted {111}B crystal facets of relatively small AlGaAs nanostructures (or nuclei), as shown in Figs. 4-10(a) and (c). As illustrated in Fig. 4-10(d), in addition, it appeared that polycrystalline “GaAs” thin layers tended to be grown on the AlGaAs nanostructures, which merged together possibly owing to the high AlGaAs coverage ratio. The hexagonal “GaAs” NWs observed in the current work have been possibly formed by the faceting growth mode, which utilizes the marked differences in the optimum growth conditions between for the six {0-11} side-wall facets and for the {111}B top ones in a conventional vapor phase growth mode (i.e., the

approximately-opposite tendency in the growth rates of the two crystal facets in terms of the growth conditions of the V/III ratio in the supplied source gas and the T_g), as similarly in the case of the NWs by SA-MOVPE [12, 13]. However, as reported in Refs. [7 - 10], it is also possible that they have been formed on relatively small AlGaAs nanostructures (or nuclei) as a result of the self-catalyzed growth by the VLS or VSS mechanism, since the self-catalyzed-grown NWs have a hexagonal prism shape similarly in the case of the NWs formed by the faceting growth mode [8]. In most of the self-catalyzed growth of III-V compound semiconductor NWs, metal droplets of the group III elements, such as Ga and In, were observed on the top of NWs after the VLS or VSS growth of NWs. However, we have observed no droplet formed on the top of our “GaAs” NWs. This might be due to the relatively high T_g of 750 °C for the MOVPE of GaAs in the current work, as shown in Fig. 1(b). Although further experiments are still required to conclude that the “GaAs” NWs have been formed on the AlGaAs nanostructure buffers, our findings in the current work show a possibility to grow semiconducting NWs on an amorphous glass substrate without any conventional metal nanoparticles, e.g., gold, as a catalyst, which are widely used in the NW formation by VLS or VSS methods.

4.8 Summary

We reported on the growth of NWs and AlGaAs nanostructures on an amorphous glass substrate using the crystallization techniques of planar amorphous Al₂O₃ interlayers deposited by ALD. On the planar Al₂O₃ interlayers deposited on the glass substrates after the anneal treatment at 975 °C in H₂ atmosphere in the MOVPE reactor, AlGaAs hexagonal nanopillars (or nanodisks) and tetrahedral nanostructures were formed in addition to AlGaAs polycrystals. Structural characterizations by XRD and TEM showed that the growth of AlGaAs {111}A or B planes was predominant even on the glass substrates. Cross-sectional lattice images obtained by TEM revealed that the crystallized γ -Al₂O₃ grains were formed in the planar Al₂O₃ interlayers

after the hydrogen annealing treatment. We observed that the $\langle 111 \rangle$ direction of the γ -Al₂O₃ crystal grains tended to be tilted against the substrate surface in the crystallized Al₂O₃ interlayers on the glass substrates. By using AlGaAs nanostructure buffers in combination with the crystallized Al₂O₃ interlayers, which included the γ -Al₂O₃ crystal grains, we realized the formation of tilted NWs on the glass substrates. No growth of AlGaAs was observed on the glass substrates without any crystallized Al₂O₃ interlayers, nor GaAs growth on the crystallized Al₂O₃ interlayers deposited on the glass substrates without any AlGaAs nanostructure buffers. The experimental results in the current work showed that the AlGaAs nanostructure buffers grown on crystallized Al₂O₃ interlayers were quite important to form semiconducting NWs on an amorphous glass substrate.

Bibliography

- [1] J. H. Choi, A. Zoukarnееv, S. I. Kim, C. W. Baik, M. H. Yang, S. S. Park, H. Suh, U. J. Kim, H. B. Son, J. S. Lee, M. Kim, J. M. Kim, and K. Kim, *Nature Photon.* **5** (2011) 763-769
- [2] V. Dhaka, T. Haggren, H. Jussila, H. Jiang, E. Kauppinen, T. Huhtio, M. Sopanen, and H. Lipsanen, *Nano Lett.* **12** (2012) 1912-1918
- [3] X. Sun, G. Calebotta, B. Yu, G. Selvaduray, and M. Meyyappan, *J. Vac. Sci. Technol. B* **25** (2007) 415-420
- [4] K. Ikejiri, F. Ishizaka, K. Tomioka, and T. Fukui, *Nanotechnology* **24** (2013) 115304
- [5] K. W. Ng, T. T. D. Tran, W. S. Ko, R. Chen, F. Lu, and C. J. Chang-Hasnain, *Nano Lett.* **13** (2013) 5931-5937
- [6] S. Jakschik, U. Schroeder, T. Hecht, M. Gutsche, H. Seidl, and J. W. Bartha, *Thin Solid Films* **425** (2003) 216-220
- [7] L. Zhang, H. C. Jiang, C. Liu, J. W. Dong, and P. Chow, *J. Phys. D: Appl. Phys.* **40** (2007) 3707-3713
- [8] C. M. Tanner, M. F. Toney, J. Lu, H. O. Blom, M. Sawkar-Mathur, M. A. Tafesse, and J. P. Chang, *J. Appl. Phys.* **102** (2007) 104112
- [9] W. E. Fenwick, N. Li, T. Xu, A. Melton, S. Wang, H. Yu, C. Summers, M. Jamil, and I. T. Ferguson, *J. Cryst. Growth* **311** (2009) 4306-4310
- [10] N. Li, S. J. Wang, C. L. Huang, Z. C. Feng, A. Valencia, J. Nause, C. Summers, and I. Ferguson, *J. Cryst. Growth* **310** (2008) 4908-4912
- [11] D. K. Biegelsen, F. A. Ponce, A. J. Smith, and J. C. Tramontana, *J. Appl. Phys.* **61** (1987) 1856-1859
- [12] S. Scholz, J. Bauer, G. Leibiger, H. Herrnberger, D. Hirsch, and V. Gottschalch, *Cryst. Res. Technol.* **41** (2006) 111-116
- [13] S. D. Wu, L. W. Guo, Z. H. Li, X. Z. Shang, W. X. Wang, Q. Huang, and J. M. Zhou, *J. Cryst. Growth* **277** (2005) 21-25

Chapter 4 Growth of semiconducting nanowire on Al₂O₃/glass substrate

[14] I. Levin and D. Brandon, *J. Am. Ceram. Soc.* **81** (1998) 1995-2012

[15] V. I. Trofimov, I. V. Trofimov, and J. I. Kim, *Thin Solid Films* **495** (2006) 398-403

[16] G. Namkoong, W. A. Doolittle, A. S. Brown, M. Losurdo, P. Capezzuto, and G. Bruno, *J. Appl. Phys.* **91** (2002) 2499-2507

[17] H. Fukuyama, K. Nakamura, T. Aikawa, H. Kobatake, A. Hakomori, K. Takada, and K. Hiraga, *J. Appl. Phys.* **107** (2010) 043502

Chapter 5 MnAs/AlGaAs nanoclusters formed on Al₂O₃/Si(111) substrates

5.1 Introduction

The intensive activities addressing the heteroepitaxy of ferromagnetic and III-V compound semiconducting layers (FM III-V hybrids) demonstrate the great interests of the semiconductor spintronics community in this subject. Due to the compatibility of these two types of materials in the hybrids, the possibility of generating new functionalities arises, which may form the basis for novel spintronic device concepts. Among all the FM III-V hybrids, the MnAs/GaAs materials system [1] has gained much attention because hexagonal NiAs-type MnAs layers and nanoclusters (NC) are ferromagnetic at room temperature or even higher temperatures [2, 3]. Magnetic logic operations were proposed using hexagonal NiAs-type MnAs thin films grown on GaAs (001) layers [4]. In addition, the ferromagnetic NiAs-type MnAs layers serve as an electrical spin injection source for semiconductors [5], and are used for lateral spin valve structures [6]. FM III-V hybrids are grown typically by molecular beam epitaxy at an extremely low growth temperature [7, 8], and devices are prepared on semiconducting substrates by using conventional top-down fabrication techniques. Granular hybrid structures in which ferromagnetic NCs are embedded into semiconductor layers are, in particular, an attractive candidate for the use in future nanospintronic devices because huge magnetoresistance (MR) effects were reported [8, 9]. However, the technological applications of these

granular hybrid structures synthesized using such conventional techniques are mainly restricted to macroscopic devices. This is due to the random distribution of the NCs in the host material, e.g., the randomness in the mean distance between the NCs, and the NC size and shape, which possibly leads to statistical fluctuations in the device characteristics [9, 10]. This issue becomes more severe with increasing the degree of miniaturization and has to be solved in the future on the way towards miniaturized devices. In addition to the efforts of creating FM III-V hybrids, ferromagnetic MnAs thin films including poly-crystals, nanoparticles, and nanowires have also intensively been investigated as candidates for possible spintronic device applications on Si substrates [11-15]. We have developed an approach, the so called selective-area metal-organic vapor phase epitaxy (SA-MOVPE), where problems due to statistical fluctuations can be avoided. SA-MOVPE is based on the bottom-up formation of single-crystalline ferromagnetic MnAs NCs on defined sites of semiconducting (111)B substrates. The SA-MOVPE technique is promising as it enables us to accurately adjust the size, shape, number, position and spatial arrangement of the ferromagnetic MnAs NCs [16-19] within the hybrid structure in order to tune its magnetic and magnetotransport properties [3, 20-22]. Ordered planar arrangements of coupled MnAs NCs show large MR effects and MR ratios of about 300% are predicted by theory [23]. However, it was observed that Mn provided during the MnAs NC growth diffused into the undoped semiconducting layers, in which it was incorporated as an acceptor yielding a p-type conductive paramagnetic diluted magnetic semiconducting layer [3]. In particular, in the case of spintronic devices where the functionality (e.g., switching) is based on a transport path through coupled MnAs NCs, shunting via the surrounding semiconducting matrix is detrimental and should be avoided. In addition, it is still difficult to grow single-crystalline ferromagnetic MnAs NCs directly on partially SiO₂-masked Si (111) substrates by our SA-MOVPE without any interlayer or buffer layer. The reason is the unintentional formation of MnSi alloys near the Si substrate surface under standard SA-MOVPE conditions, in particular, at the relatively high growth temperature of 800 °C used in the SA-MOVPE growth of MnAs NCs [24].

In this chapter, we offer a solution to the problem of shunting and report on the formation and

magnetic characterization of ferromagnetic MnAs NCs on nanostructured AlGaAs buffers grown by SA-MOVPE using a thin crystallized Al₂O₃ insulating interlayer prepared by atomic layer deposition (ALD) on a Si (111) substrate. The use of the Al₂O₃ layers enables us to prevent the unintentional Mn diffusion into the semi-insulating substrate and thus the formation of a shunting channel. We previously used the crystallization techniques of thin amorphous Al₂O₃ layers deposited by ALD as interlayers on amorphous glass substrates to promote the nucleation before the growth of the semiconducting AlGaAs nanostructures [25]. It was also reported that thin amorphous Al₂O₃ layers prepared by ALD crystallized after an annealing treatment at a relatively high temperature [26-28]. Furthermore, the epitaxial growth of semiconductors on Al₂O₃ layers prepared on single-crystalline substrates by ALD was demonstrated, e.g., GaN growth on a Si (111) substrate and InGaN growth on a ZnO (0001) substrate with Al₂O₃ interlayers [29, 30]. Being able to electrically isolate the NCs grown by SA-MOVPE from the underlying semiconducting layers comprises an important step towards making such FM III-V hybrids promising candidates for a use in spintronics. Such NCs can be used as building blocks for future magneto-nanoelectronic or spintronic devices, such as magnetic logic circuits, memories, and sensors, that will be fabricated on semiconducting substrates in a reproducible manner, as discussed in the review paper for MnAs NC [31].

5.2 Experimental procedures

For the growth of the NC arrangements by SA-MOVPE, first, a thin amorphous Al₂O₃ layer was deposited by ALD on a Si (111) substrate at a temperature of 300 °C with (CH₃)₃Al, and H₂O as precursors. The thickness of the amorphous Al₂O₃ layers was approximately 5 nm for the samples studied by cross-sectional TEM and 10 nm for the samples used for the SA-MOVPE of the MnAs/AlGaAs NCs. We deposited thicker Al₂O₃ layers (10 nm) for the samples used for the NC growth to ensure that pin-hole free Al₂O₃ layers are obtained after the annealing treatment to prevent the precursors for the AlGaAs and MnAs

growth from directly reaching the Si (111) substrate surface. After the deposition, we annealed the Si (111) substrates with the deposited Al₂O₃ layers in N₂ atmosphere at 900 °C for 3 minutes in a rapid thermal annealing (RTA) system in order to crystallize the amorphous Al₂O₃ layers. In the next step, the Al₂O₃ layers crystallized on Si (111) substrates were covered with a pre-patterned growth-inhibiting SiO₂ mask layer using plasma-enhanced chemical vapor deposition, electron beam lithography, and wet chemical etching by buffered HF (BHF) solution. The first annealing treatment is very important to prevent the etch-off of the Al₂O₃ layers by BHF solution for the substrate preparation process of SA-MOVPE. We experimentally confirmed that there was almost no change in the thickness of the Al₂O₃ layers after the annealing treatment at temperatures higher than 900 °C before and after the wet chemical etching using BHF solution. (In contrast, as-deposited amorphous Al₂O₃ layers by ALD and the Al₂O₃ layers after the annealing treatment in N₂ atmosphere at 800 °C in the RTA system were etched off by BHF solution.) The mask openings were formed in a regular circular-shape with a diameter of 200 nm and in an elongated line shape with a width of 200 nm and a length of 10 μm. The elongation directions were oriented along one of the <0-11> directions of the Si (111) substrate. For the SA-MOVPE, the estimated partial pressures of (CH₃)₃Ga, (CH₃)₃Al, (MeCp)₂Mn and AsH₃ in the MOVPE reactor were approximately [(CH₃)₃Ga] = 2.0 × 10⁻⁶, [(CH₃)₃Al] = 3.3 × 10⁻⁷, and [AsH₃] = 1.2 × 10⁻³ atm for the AlGaAs buffer layer growth, and [(MeCp)₂Mn] = 5.2 × 10⁻⁷ and [AsH₃] = 5.8 × 10⁻⁴ atm for the MnAs NC growth, respectively. Before the growth of the AlGaAs buffer layers, the samples were annealed a second time at 975 °C for 10 minutes in H₂ atmosphere in the MOVPE reactor. Only H₂ was introduced into the MOVPE reactor during cooling down to 400 °C, prior to growing the AlGaAs buffer layers. At this temperature, the growth of the buffers commenced and lasted for 3 minutes, before the temperature was raised further to 750 °C where the growth continued for another 3 minutes. Afterwards, the MnAs NCs were grown at 750 °C for 15 minutes and formed only on the AlGaAs buffer layers grown on the Al₂O₃ layer surface in the SiO₂ mask openings.

5.3 Selective-area growth of MnAs/AlGaAs nanoclusters on Al₂O₃/Si(111)

Size and crystal facets of the MnAs NCs were investigated by scanning electron microscopy (SEM). Lattice images of the crystallized Al₂O₃ layers were examined by cross-sectional TEM. We characterized the magnetic domain structures of the MnAs NCs and the coupled NCs by MFM under zero magnetic field conditions at room temperature after applying an external magnetic field, \mathbf{B} , of 1,000 Gauss. Electrical contacts were prepared using electron beam lithography followed by thermal evaporation of Ti (10 nm) and Au (100 nm). An external magnetic field, \mathbf{B} , was applied neither before nor during the measurements. The temperature dependence of the resistance of coupled MnAs NCs was measured from 144 to 175 K. The temporal dependence of the resistance was investigated in detail at 152 K, as, at this temperature, the resistivity jumps could be recorded with a good statistics.

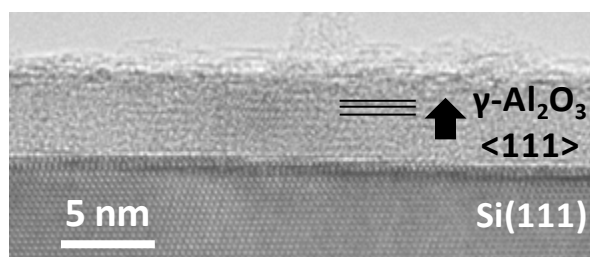


Fig. 5-1 Cross-sectional transmission electron microscopy lattice image of the sample of a planar 5-nm-thick Al₂O₃ layer deposited on a Si (111) substrate after the AlGaAs growth (No observable nanostructured AlGaAs buffers are in the observed region). No SiO₂ mask layer was deposited on the Al₂O₃ layers.

Results of the investigation of the Al₂O₃ layers on Si (111) substrates by TEM after the annealing treatment only at 975 °C for 10 minutes in H₂ atmosphere in the MOVPE reactor are given in Fig. 5-1. It depicts a cross-sectional TEM lattice image taken with an electron-beam injection perpendicular to one of the {0-11} crystal planes of a Si (111) substrate. Lattice fringes which are approximately parallel to the Si (111) substrate planes are markedly observed in a wide area of the Al₂O₃ layer. It was estimated by fast Fourier transform (FFT) of the observed lattice images that these lattice fringes were attributable to a lattice spacing

of 0.46 nm, which was in good agreement with the well-known literature value of 0.456 nm for the {111} planes of γ -Al₂O₃ (from the JCPDS database). Therefore, it is reasonable to assume that the crystal structure of grains observed in the Al₂O₃ layers is γ -Al₂O₃. In the case of poly-crystalline γ -Al₂O₃ grains in Al₂O₃ layers deposited on amorphous glass substrates,²⁵ we observed that some of the {111} planes of γ -Al₂O₃ were tilted against the amorphous glass substrate planes. Therefore, we conclude that the $\langle 111 \rangle$ direction of γ -Al₂O₃ layers studied here exhibits a marked epitaxial relationship with, i.e., is parallel to, the $\langle 111 \rangle$ direction of the Si (111) substrates in the current study.

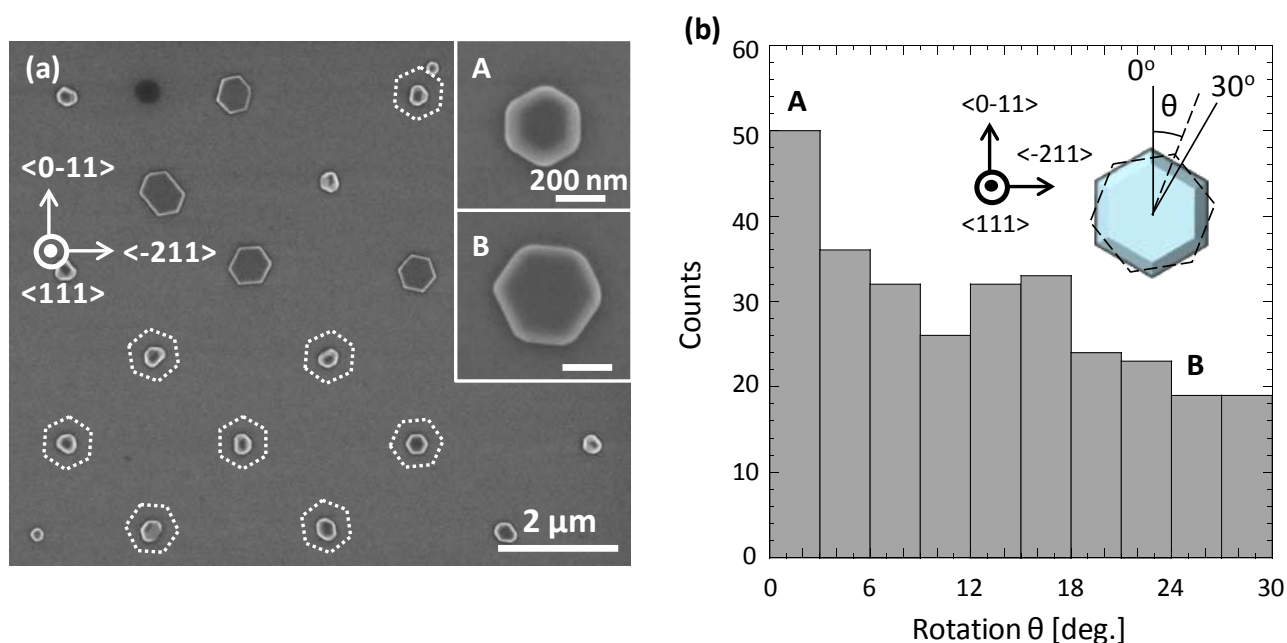


Fig. 5-2 (a) Top view of scanning electron microscopy image of the sample after the MnAs growth in the circular SiO₂ mask openings with a diameter of 200 nm. The insets are top views of highly-magnified scanning electron microscopy images of typical MnAs nanoclusters. White scale bars in the insets represent 200 nm. (b) Histogram of the distribution of the rotation angle, θ , for MnAs nanoclusters against the $\langle 0-11 \rangle$ direction of the Si (111) substrate.

SA-MOVPE growth of hexagonal MnAs NCs on such Al₂O₃/Si (111) substrates was carried out after the selective-area growth of an AlGaAs buffer layer. Figure 5-2(a) shows a typical top view of the regular hexagonal MnAs NC arrays. We observe that the hexagonal disks are randomly oriented along the $\langle 111 \rangle$ direction of the Si substrate, as indicated by white dotted hexagons in the Figure 5-2. We conclude that these hexagonal NCs are MnAs as MFM measurements yield a noticeable magnetic response and confirm the formation of magnetic domains at room temperature after applying a \mathbf{B} of 1,000 Gauss (not shown here). The insets show two types of typical NCs marked “A” and “B”. In our previous study related to the SA-MOVPE of MnAs NCs on GaAs (111)B substrates[18], it was found that the hexagons of the MnAs NCs, which arise from the NiAs-type crystal structure, were always rotated by 30° against those of the AlGaAs buffer layer underneath. The corresponding hexagonal nanodisk structure of the AlGaAs buffer layer exhibits six equivalent $\{0-11\}$ side-wall facets. The same holds for NCs of type “A” in the inset of Fig. 5-2(a). Therefore, MnAs NCs of type “A” possess presumably a similar structure as the MnAs NCs grown on GaAs (111)B substrates. In this case, it should be noted that the c-axis, i.e., the $\langle 0001 \rangle$ direction, of the MnAs NCs is parallel to both of the $\langle 111 \rangle$ directions of the γ -Al₂O₃ layer and the Si (111) substrate. Other MnAs NCs, e.g., those of type “B” show a different in-plane orientation. We summarize the observed tendency of the NC rotation, θ , against the $\langle 0-11 \rangle$ direction of the Si substrate in a histogram shown in Fig. 5-2(b). The NCs denoted by “A” and “B” in the insets of Fig. 5-2(a) represent typical NCs marked in the bars “A” and “B” in the histogram of Fig. 5-2(b). The NCs denoted by “A” in the inset of Fig. 5-2(a) show the highest occurrence probability, i.e., 17% (50 counts in the total counts of 294 on the observed samples). We conclude that, in the crystallized Al₂O₃ layers, the $\{111\}$ planes of the γ -Al₂O₃ grains are possibly somewhat rotated about the $\langle 111 \rangle$ axis at random despite there is the epitaxial relationship between γ -Al₂O₃ and the Si $\{111\}$ planes. It is also possible that the $\{111\}$ planes of the γ -Al₂O₃ layer are tilted against the Si $\{111\}$ substrate plane. However, the results shown in the histogram seem to be consistent with the results of the cross-sectional TEM observation, which confirm that almost all the observed lattice fringes of γ -Al₂O₃ are approximately parallel to the Si (111) substrate planes.

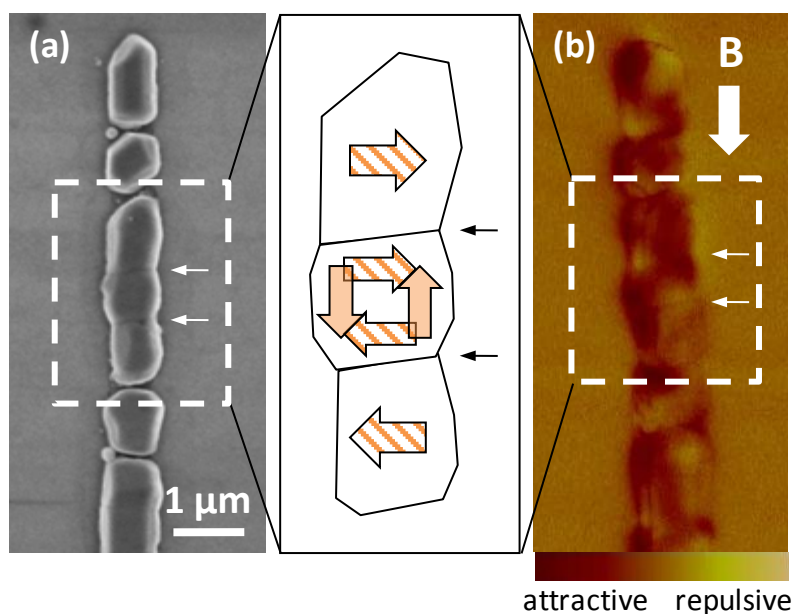


Fig. 5-3 (a) Scanning electron and (b) magnetic force microscopy images of MnAs nanoclusters grown in an elongated line-shaped SiO₂ mask opening with a width of 200 nm and a length of 10 μm. Two white arrows in the figures represent the interfaces between the coupled MnAs NCs.

5.4 Magnetic characterization by MFM observations

In the case of the elongated line-like mask openings, we have not obtained uniform lateral MnAs nanowires, but a kind of chain structure of MnAs NCs of different sizes and shapes aligned parallel to the $\langle 0-11 \rangle$ direction of the elongated mask openings on the Si substrate. This might be due to the only partial crystalline character of the Al₂O₃ layers on the length scale of the relatively long elongated mask opening of 10 μm. This appears to be a likely reason because we have observed the formation of lateral MnAs nanowires with lengths of 5 μm or longer on single-crystalline AlGaAs buffer layers grown in similar SiO₂ mask openings on GaAs (111)B substrates in a previous work [32]. As shown in Fig. 5-3(a), some of the NCs have an elongated or almost regular polygonal shape with well-defined crystal facets, although the size uniformity of the NCs is rather poor, while others are probably poly-crystalline without any marked crystal

facets. Figure 5-3(b) shows an MFM image of the same structure presented in Fig. 5-3(a) recorded at room temperature after applying $\mathbf{B} = 1,000$ Gauss along the direction indicated by the white arrow in the figure. For the arrangement consisting of three NCs marked by the white broken rectangle in the middle of Fig. 5-3(a), we observe four magnetic domains, i.e., a single magnetic domain for each of the outer two NCs and two magnetic domains for the NC in the center of the arrangement. The two white arrows in Fig. 5-3(a) represent the interfaces between the coupled MnAs NCs. For the outer two NCs, it seems that their magnetization directions are oriented perpendicular to the applied \mathbf{B} direction, i.e., the applied magnetic field strength seems to be insufficient to align the magnetic domains of the NCs. The centered NC with an almost regular polygonal shape seems to consist of two magnetic domains, whose magnetizations are oriented in an anti-parallel configuration. The two possibilities for the anti-parallel alignment are illustrated in the schematic image.

5.5 Leakage current measurement

In order to check if there are leak path for the current, we measured current-voltage characteristics of the area where MnAs nanoclusters or Al₂O₃ layers exposed and SiO₂ layer was uncovered. We used needle-setup and checked with a two-needle measurement. Figure 5-4 shows overview of the measurement. We found a negligible current $< 10^{-10}$ A, so from this measurements, we can assume, that the Al₂O₃ layer is enough insulating.

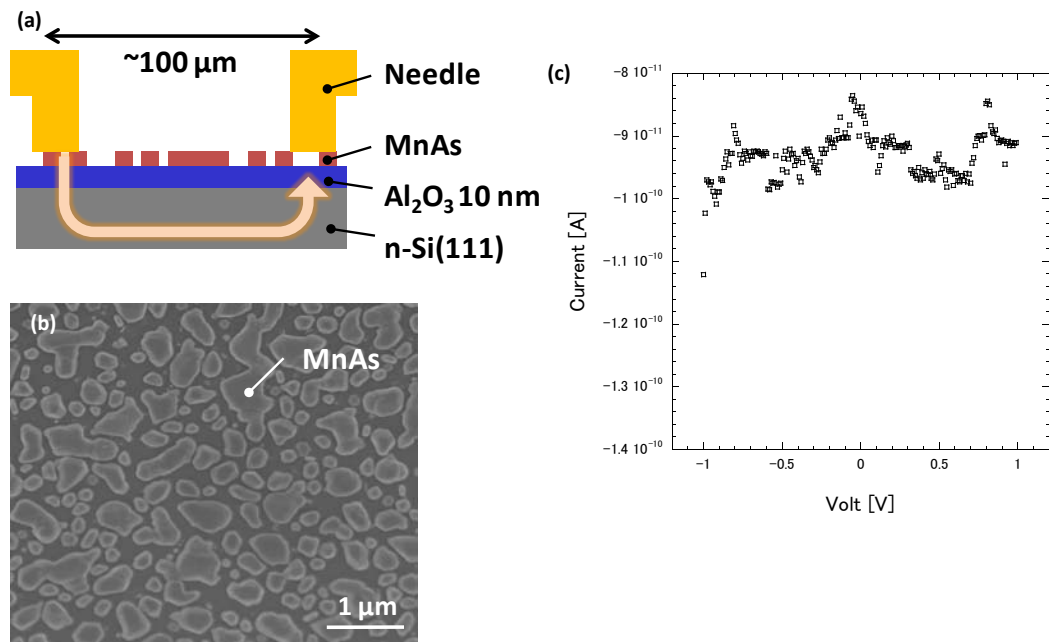


Fig. 5-4 (a) Schematic illustration of setup for leakage current measurement. (b) SEM image of typical surface morphology where needles were put on. (c) Current-voltage characteristics of the area where MnAs nanoclusters or Al₂O₃ layers exposed and SiO₂ layer was uncovered.

5.6 Electrical characteristic of coupled MnAs nanocluster arrangement

Finally, after the two-terminal device fabrication process, we measured the temperature and temporal dependences of the resistance for a small number of coupled MnAs NCs. A top view SEM image of the MnAs NC arrangement investigated is shown in the inset of Fig. 5-4 (a). The arrangement consists of three MnAs NCs oriented along the $\langle 0-11 \rangle$ direction of the Si substrate, which are located between the two electrodes fabricated. Two NCs exhibit an almost regular polygonal shape while in between two NCs completely merged during the growth process forming a long elongated NC with a constriction in its center. Two white arrows in the inset of Fig. 5-4(a) denote the possible interfaces between the coupled MnAs NCs.

Figure 5-4 (a) shows the temperature dependence of the resistance, R , which decreases with increasing the measurement temperature from 144 to 175 K. In addition, discrete jumps in the resistance marked by black arrows in Fig. 5-4(a) are observed in a narrow temperature range, which occur more frequently when the

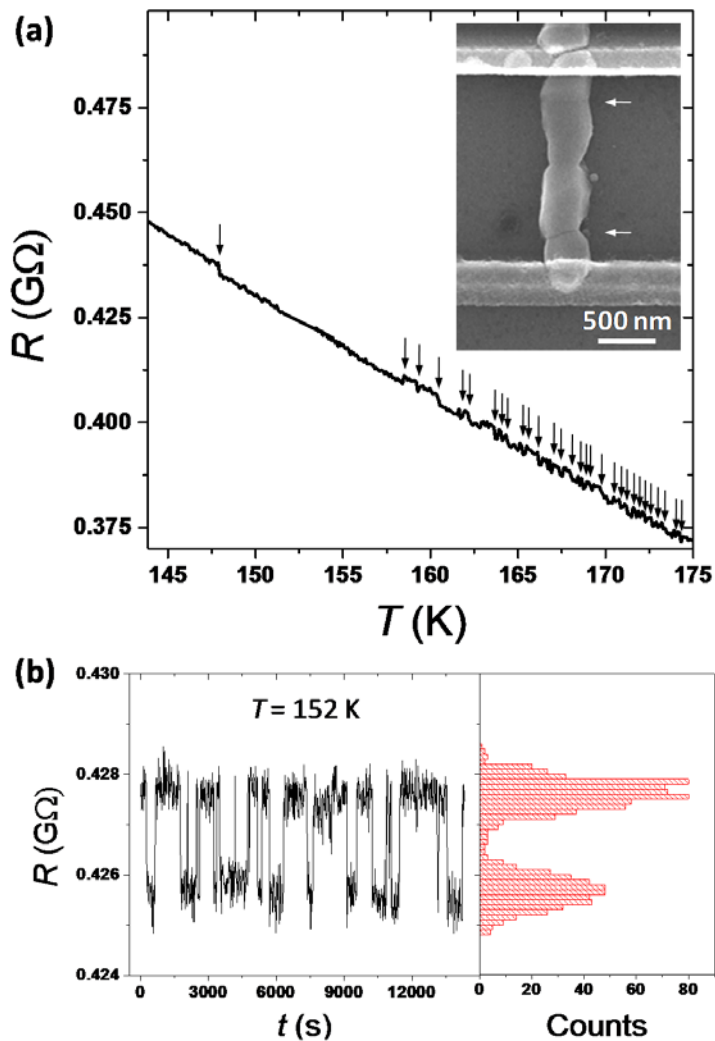


Fig. 5-4 (a) Temperature dependence of the resistance of coupled MnAs nanoclusters from 144 to 175 K. Arrows in the figure show the positions at which the resistance jumps between high and low resistance levels. The inset shows a scanning electron microscopy image of the coupled MnAs nanoclusters measured. Two white arrows in the inset of Fig. 4(a) represent the interfaces between the coupled MnAs NCs. (b) Observed random telegraph noise of coupled MnAs nanoclusters at a specific temperature of 152 K. The histogram summarizes the count distribution of the resistance values from the temporal dependence of the resistance at 152 K.

temperature is increased. Figure 5-4(b) shows the temporal dependence of the resistance for the coupled MnAs NCs at an intermediate temperature of 152 K. The temporal dependence of R as well as the histogram of the resistance levels shown in Fig. 5-4(b) clearly demonstrate that the NC arrangement exhibits magnetic random telegraph noise, where the resistance fluctuates between two discrete resistance levels. As shown in our previous study reported in Ref. 22, the magnetic random telegraph noise can be attributed to thermally activated changes of the magnetic structure of coupled MnAs NCs, such as switching of a small magnetic domain or thermal fluctuations of the magnetic domain wall between different domains. The observed behavior can be understood qualitatively by assuming that the NC arrangement consists of different magnetic domains, which is in accordance with the observations by MFM [22, 32]. Assuming a similar magnetic domain structure as observed by MFM investigations of the comparable NC arrangement shown in Fig. 5-3(b), the NC arrangement investigated may exhibit a complex magnetic domain structure, i.e., a single magnetic domain for each of the NCs or even two magnetic domains in one single NC. As the shape of the outer NCs is almost regular polygonal, no strong magnetic shape anisotropy is expected. Assuming single magnetic domain character of all the three NCs, the discrete jumps between two resistance levels shown in Fig. 5-4 may then be caused by thermally activated changes of the magnetization orientation in the NC with an almost polygonal shape or of the domain walls between the domains, while, for the elongated NC with a constriction in its middle part, the magnetization may be fixed due to a relatively strong magnetic shape anisotropy. However, a detailed investigation of the magnetic random telegraph noise is needed in order to establish a complex magnetic structure. We believe that an even better control of the magnetic domain structures may be achieved after further optimization of the crystallization processes of the amorphous Al₂O₃ layers to build MR devices fabricated by our bottom-up approach of selective-area growth on Si (111) substrates.

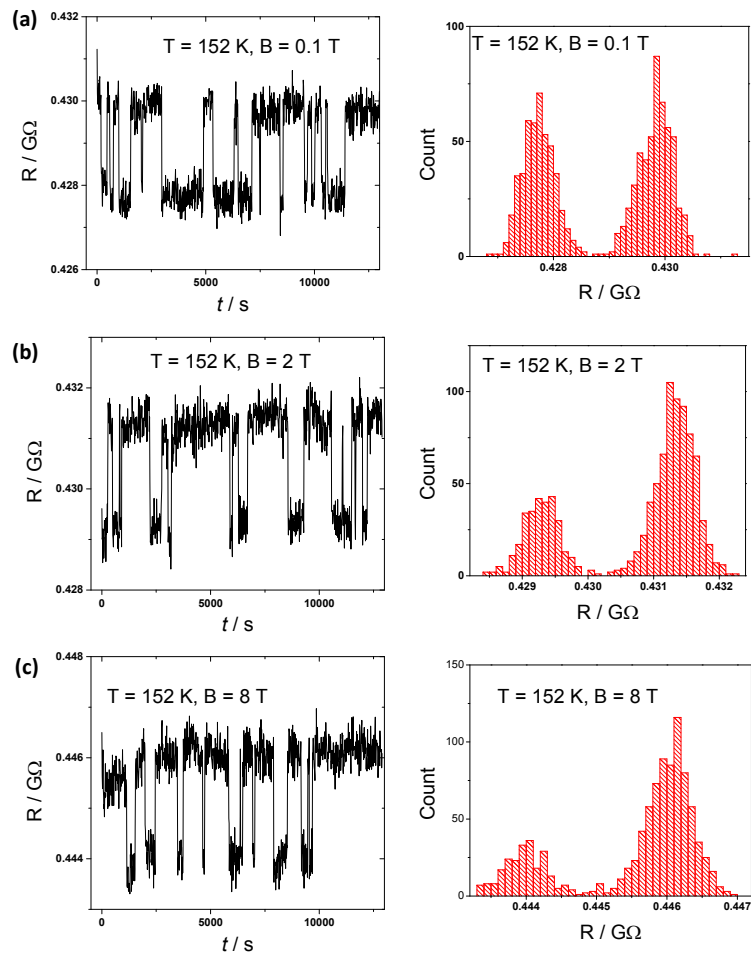


Fig. 5-6 External magnetic field dependence of random telegraph noise measurement. Magnetic field applied along the $\langle 0-11 \rangle$ direction. $T = 152$ K. (a) $B = 0.1$ T, (b) $B = 2$ T, (c) $B = 8$ T.

Subsequently, we applied external magnetic field along the $\langle 0-11 \rangle$ (Fig. 5-6) and $\langle -211 \rangle$ (Fig. 5-7) direction of Si(111) substrate and conducted time dependent measurement. External magnetic field ranged 0.1 to 8 T. In the measurement for the $\langle 0-11 \rangle$ direction, we applied 0.1 (Fig. 5-6(a)), 2 (Fig. 5-6(b)), and 8 (Fig. 5-6(c)) T. Magnetic random telegraph noise were appeared in all magnetic field. The histograms revealed that the counts of high resistance level increase with increasing applied magnetic field. In the measurement for the $\langle -211 \rangle$ direction, we applied 0.1 (Fig. 5-7(a)), 0.25 (Fig. 5-7(b)), and 1 (Fig. 5-7(c)) T. Random telegraph noises were also appeared. The amplitudes of random telegraph noise were obviously higher than the measurement in the case of $\langle 0-11 \rangle$ direction. As shown in our previous study reported in Ref. 22, the magnetic random telegraph noise disappeared when external magnetic field was applied in more than

3 T. The reason why random telegraph noise disappear is explained that a small magnetic domain which cause random telegraph noise become fixed in consequence of external magnetic field. In this study, The differences from our previous study reported in Ref. 22 are insulated from substrate, and polycrystalline because of MnAs nanoclusters fabricated on Al₂O₃/Si(111) substrate. These differences might affect the appearance of random telegraph noise under external magnetic field.

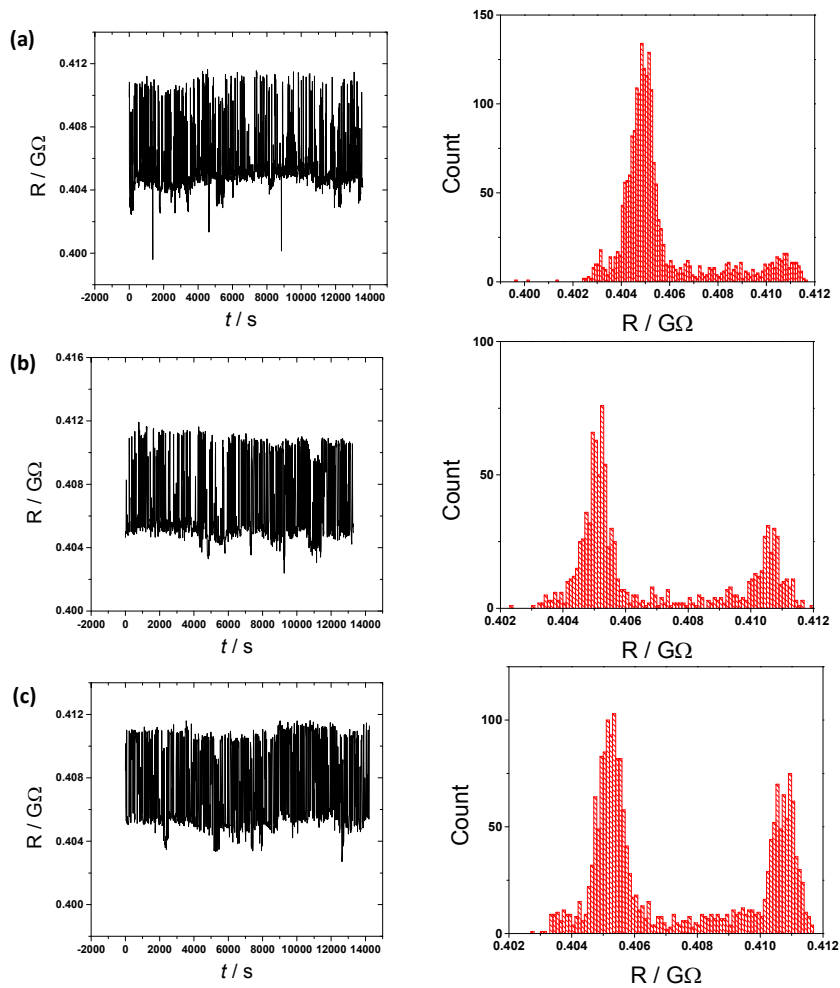


Fig. 5-6 External magnetic field dependence of random telegraph noise measurement. Magnetic field applied along the $\langle 0-11 \rangle$ direction. $T = 152$ K. (a) $B = 0.1$ T, (b) $B = 2$ T, (c) $B = 8$ T.

Bibliography

- [1] R. Engel-Herbert, T. Hesjedal, D. M. Schaadt, L. Däweritz, and K. H. Ploog, *Appl. Phys. Lett.* **88**, 052505 (2006).
- [2] F. Ishikawa, K. Koyama, K. Watanabe, and H. Wada, *Jpn. J. Appl. Phys.* **42**, L918 (2003).
- [3] M. T. Elm, C. Michel, J. Stehr, D. M. Hofmann, P. J. Klar, S. Ito, S. Hara, and H.-A. Krug von Nidda, *J. Appl. Phys.* **107**, 013701 (2010).
- [4] P. Pampuch, A. K. Das, A. Ney, L. Däweritz, R. Koch, and K. H. Ploog, *Phys. Rev. Lett.* **91**, 147203 (2003).
- [5] M. Ramsteiner, H. Y. Hao, A. Kawaharazuka, H. J. Zhu, M. Kästner, R. Hey, L. Däweritz, H. T. Grahn, and K. H. Ploog: *Phys. Rev. B* **66**, 081304(R) (2002).
- [6] D. Saha, M. Holub, P. Bhattacharya, and Y. C. Liao: *Appl. Phys. Lett.* **89**, 142504 (2006).
- [7] V. Garcia, H. Jaffrès, J.-M. George, M. Marangolo, M. Eddrief, and V. H. Etgens, *Phys. Rev. Lett.* **97**, 246802 (2006).
- [8] S. Sugahara and M. Tanaka, *Appl. Phys. Lett.* **80**, 1969 (2002).
- [9] P. N. Hai, S. Ohya, M. Tanaka, S. E. Barnes, and S. Maekawa, *Nature* **458**, 489 (2009).
- [10] C. Michel, M. T. Elm, B. Goldlücke, S. D. Baranovskii, P. Thomas, W. Heimbrod, and P. J. Klar, *Appl. Phys. Lett.* **92**, 223119 (2008).
- [11] K. Akeura, M. Tanaka, T. Nishinaga, and J. De Boeck, *J. Appl. Phys.* **79**, 4957 (1996).
- [12] A. M. Nazmul, A. G. Banskchikov, H. Shimizu, and M. Tanaka, *J. Cryst. Growth* **227-228**, 874 (2001).
- [13] M. Solzi, C. Pernechele, M. Ghidini, M. Natali, and M. Bolzan, *J. Magn. Magn. Mater.* **322**, 1565 (2010).

- [14] M. F. H. Wolff, D. Görlitz, K. Nielsch, M. E. Messing, and K. Deppert, *Nanotechnology* **22**, 055602 (2011).
- [15] J. Sadowski, A. Siusys, A. Kovacs, T. Kasama, R. E. Dunin-Borkowski, T. Wojciechowski, A. Reszka, and B. Kowalski, *Phys. Status Solidi B* **248**, 1576 (2011).
- [16] S. Hara, D. Kawamura, H. Iguchi, J. Motohisa, and T. Fukui, *J. Cryst. Growth* **310**, 2390 (2008).
- [17] S. Ito, S. Hara, T. Wakatsuki, and T. Fukui, *Appl. Phys. Lett.* **94**, 243117 (2009).
- [18] K. Komagata, S. Hara, S. Ito, and T. Fukui, *Jpn. J. Appl. Phys.* **50**, 06GH01 (2011).
- [19] S. Hara and K. Komagata, *Phys. Status Solidi B* **252**, 1925 (2015).
- [20] M. T. Elm, P. J. Klar, S. Ito, and S. Hara, *Phys. Rev. B* **83**, 235305 (2011).
- [21] M. T. Elm, P. J. Klar, S. Ito, S. Hara, and H.-A. Krug von Nidda, *Phys. Rev. B* **84**, 035309 (2011).
- [22] M. Fischer, M. T. Elm, H. Kato, S. Sakita, S. Hara, and P. J. Klar. *Phys. Rev. B* **92**, 165306 (2015).
- [23] C. Heiliger, M. Czerner, P. J. Klar, and S. Hara, *IEEE Trans. Magn.* **46**, 1702 (2010).
- [24] S. Hara and K. Morita, in preparation for submission.
- [25] S. Sakita and S. Hara, *Jpn. J. Appl. Phys.* **54**, 075504 (2015).
- [26] S. Jakschik, U. Schroeder, T. Hecht, M. Gutsche, H. Seidl, and J. W. Bartha, *Thin Solid Films* **425**, 216 (2003).
- [27] L. Zhang, H. C. Jiang, C. Liu, J. W. Dong, and P. Chow, *J. Phys. D* **40**, 3707 (2007).
- [28] C. M. Tanner, M. F. Toney, J. Lu, H. O. Blom, M. Sawkar-Mathur, M. A. Tafesse, and J. P. Chang, *J. Appl. Phys.* **102**, 104112 (2007).
- [29] W. E. Fenwick, N. Li, T. Xu, A. Melton, S. Wang, H. Yu, C. Summers, M. Jamil, and I. T. Ferguson, *J. Cryst. Growth* **311**, 4306 (2009).
- [30] N. Li, S. J. Wang, C. L. Huang, Z. C. Feng, A. Valencia, J. Nause, C. Summers, and I. Ferguson, *J. Cryst. Growth* **310**, 4908 (2008).
- [31] M. T. Elm and S. Hara, *Adv. Mater.* **26**, 8079 (2014).
- [32] H. Kato, S. Sakita, and S. Hara, *J. Cryst. Growth* **414**, 151 (2015).

Chapter 6 Conclusion

In Chapter 4, we reported on the growth of NWs and AlGaAs nanostructures on an amorphous glass substrate using the crystallization techniques of planar amorphous Al_2O_3 interlayers deposited by ALD. On the planar Al_2O_3 interlayers deposited on the glass substrates after the anneal treatment at 975 °C in H_2 atmosphere in the MOVPE reactor, AlGaAs hexagonal nanopillars (or nanodisks) and tetrahedral nanostructures were formed in addition to AlGaAs polycrystals. Structural characterizations by XRD and TEM showed that the growth of AlGaAs {111}A or B planes was predominant even on the glass substrates. Cross-sectional lattice images obtained by TEM revealed that the crystallized $\gamma\text{-Al}_2\text{O}_3$ grains were formed in the planar Al_2O_3 interlayers after the hydrogen anneal treatment. We observed that the $\langle 111 \rangle$ direction of the $\gamma\text{-Al}_2\text{O}_3$ crystal grains tended to be tilted against the substrate surface in the crystallized Al_2O_3 interlayers on the glass substrates. By using AlGaAs nanostructure buffers in combination with the crystallized Al_2O_3 interlayers, which included the $\gamma\text{-Al}_2\text{O}_3$ crystal grains, we realized the formation of tilted NWs on the glass substrates. No growth of AlGaAs was observed on the glass substrates without any crystallized Al_2O_3 interlayers, nor GaAs growth on the crystallized Al_2O_3 interlayers deposited on the glass substrates without any AlGaAs nanostructure buffers. The experimental results in the current work showed that the AlGaAs nanostructure buffers grown on crystallized Al_2O_3 interlayers were quite important to form semiconducting NWs on an amorphous glass substrate.

In Chapter 5, We report on selective-area metal-organic vapor phase epitaxy and magnetic characterization of coupled MnAs/AlGaAs nanoclusters formed on thin Al₂O₃ insulating layers crystallized on Si (111) substrates. Cross-sectional transmission electron microscopy reveals that poly-crystalline γ -Al₂O₃ grains are formed after an annealing treatment of the amorphous Al₂O₃ layers deposited by atomic layer deposition on Si (111) substrates. The $\langle 111 \rangle$ direction of the γ -Al₂O₃ grains tends to be oriented approximately parallel to the $\langle 111 \rangle$ direction of the Si substrate. We observe that hexagonal MnAs nanoclusters on AlGaAs buffer layers grown by selective-area metal-organic vapor phase epitaxy on partially SiO₂-masked Al₂O₃ insulator crystallized on Si (111) substrates are oriented with the c-axis along the $\langle 111 \rangle$ direction of the substrates, but exhibit a random in-plane orientation. A likely reason is the random orientation of the poly-crystalline γ -Al₂O₃ grains in the Al₂O₃ layer plane. Magnetic force microscopy studies at room temperature reveal that arrangements of coupled MnAs nanoclusters exhibit a complex magnetic domain structure. Such arrangements of coupled MnAs nanoclusters may also show magnetic random telegraph noise, i.e. jumps between two discrete resistance levels, in a certain temperature range, which can be explained by thermally activated changes of the complex magnetic structure of the nanocluster arrangements.

List of Publications

1. Publications related to this work

Journals

- [1] S. Sakita, and S. Hara: "Growth of AlGaAs nanostructures on crystallized Al₂O₃ interlayers for semiconducting nanowire growth on glass substrate", Japanese Journal of Applied Physics, 54, No. 7, pp. 075504-1-8, 2015. (IF=1.127, TC=0)
- [2] S. Sakita, S. Hara, M. T. Elm, and P. J. Klar: "Selective-area growth and magnetic characterization of MnAs/AlGaAs nanoclusters on insulating Al₂O₃ layers crystallized on Si (111) substrates", Applied Physics Letters, in press, 2016.

Conference proceedings

- [3] S. Sakita, M. Yatago, and S. Hara: "Growth and Characterization of AlGaAs Nanowires on Insulating Al₂O₃ Layers by Selective-Area Metal-Organic Vapor-Phase Epitaxy", the 2012 International Conference on Solid State Devices and Materials (SSDM 2012), Kyoto, Japan, September 25-27, C-2-5, pp. 664-665 (2012).
- [4] S. Sakita, M. Yatago, and S. Hara: "Selective-Area Metal-Organic Vapor-Phase Epitaxy of AlGaAs Nanostructures on Crystallized Insulating Al₂O₃ Layers", the 25th International Microprocesses and Nanotechnology Conference (MNC 2012), Kobe, Japan, October 30-November 2, pp. 31C-2-5-1-31C-2-5-2 (2012).
- [5] S. Sakita, H. Kato, and S. Hara: "Selective-Area Growth of AlGaAs Nanostructures on Al₂O₃/Glass Substrate", the 17th International Conference on Metal-Organic Vapor Phase Epitaxy (ICMOVPE-XVII), Lausanne, Switzerland, July 13-18, p. Mon-Poster-2-25-1 (2014).

2. Publications related to other work

- [1] M. Yatago, H. Iguchi, S. Sakita, and S. Hara: "Growth and Characterization of MnAs Nanoclusters Embedded in GaAs Nanowires by Metal-Organic Vapor Phase Epitaxy", Japanese Journal of Applied Physics, Vol. 51, No. 2, pp. 02BH01-1-8, 2012. (IF=1.127, TC=7)
- [2] S. Hara, S. Sakita, and M. Yatago: "Selective-Area Growth and Electrical Characterization of Hybrid Structures between Semiconducting GaAs Nanowires and Ferromagnetic MnAs Nanoclusters", Japanese Journal of Applied Physics, Vol. 51, No. 11, pp. 11PE01-1-7, 2012 (IF=1.127, TC=4)
- [3] Y. Kohashi, S. Sakita, S. Hara, and J. Motohisa: "Pitch-Independent Realization of 30-nm-Diameter InGaAs Nanowire Arrays by Two-Step Growth Method in

Selective-Area Metal-Organic Vapor Phase Epitaxy”, Applied Physics Express, Vol. 6, No. 2, pp. 025502-1-3, 2013. (IF=2.365, TC=2)

- [4] S. Hara, H. Fujimagari, S. Sakita, and M. Yatago: “Difference in Formation of Ferromagnetic MnAs Nanoclusters on III-V Semiconducting Nanowire Templates”, (**Conference Proceedings**) Proceedings of SPIE, Vol. 8820, pp. 88200V-1-88200V-12 (SPIE, Bellingham, Washington, 2013)
- [5] M. Fischer, M. T. Elm, S. Sakita, S. Hara and P. J. Klar: "Magnetoresistance effects and spin-valve like behavior of an arrangement of two MnAs nanoclusters", Applied Physics Letters Vol. 106, pp. 032401-1 -5, 2015 (IF=3.302, TC=3)
- [6] H. Kato, S. Sakita, S. Hara: "Selective-area growth and magnetic characterization of lateral MnAs nanowires", Journal of Crystal Growth Vol. 414, pp. 151-155, 2015. (IF=1.698, TC=1)
- [7] M. Fischer, M. T. Elm, H. Kato, S. Sakita, S. Hara and P. J. Klar: "Analysis of magnetic random telegraph noise in individual arrangements of a small number of coupled MnAs nanoclusters", Physical Review B Vol. 92, pp. 165306-1-7, 2015 (IF=3.736, TC=0)

3. Presentations related to this work

International conference

- [1] S. Sakita and S. Hara: “Growth of AlGaAs Nanowires on Planar Al₂O₃ Layers Deposited on Si (111) and Amorphous Glass Substrates”, the 2014 Materials Research Society (MRS) Spring Meeting, San Francisco, California, USA, April 21-25, 2014, UU3.18.

Domestic conference

- [1] 崎田 晋哉, 原 真二郎: 「Al₂O₃ 絶縁膜上の横型MnAsナノワイヤの作製と評価」, 第 76 回応用物理学会秋季学術講演会, 名古屋, 2015 年 9 月
- [2] 崎田 晋哉, 加藤 弘晃, 原 真二郎: 「Al₂O₃ 中間層を用いた非晶質ガラス上のAlGaAs ナノ構造のMOVPE選択成長」, 第 61 回応用物理学会春季学術講演会, 相模原, 2014 年 3 月.
- [3] 崎田 晋哉, 加藤 弘晃, 原 真二郎: 「ALDで堆積したAl₂O₃ 中間層を用いた非晶質ガラス上のAlGaAsナノ構造の作製と評価」, 第 49 回応用物理学会北海道支部/第 10 回日本光学会北海道地区合同学術講演会, 札幌, 2013 年 12 月.
- [4] 崎田 晋哉, 藤曲 央武, 原 真二郎: 「Si (111)及び非晶質ガラスに堆積したAl₂O₃ 膜上のAlGaAsナノ構造の作製と評価」, 第 74 回応用物理学会秋季学術講演会, 京都, 2013 年 9 月.
- [5] 崎田 晋哉, 藤曲 央武, 原 真二郎: 「MOVPE選択成長法によるAl₂O₃ 絶縁膜上のAlGaAsナノワイヤの作製と評価」, 第 60 回応用物理学会春季学術講演会, 厚木, 2013 年 3 月.

- [6] 崎田 晋哉, 藤曲 央武, 原 真二郎: 「SA-MOVPE法による Al_2O_3 絶縁膜上のAlGaAsナノ構造の成長と評価」, 第48回応用物理学会北海道支部/第9回日本光学会北海道地区合同学術講演会, 釧路, 2013年1月.
- [7] 崎田 晋哉, 矢田郷 昌稔, Matthias Thomas Elm, 原 真二郎: 「 Al_2O_3 絶縁膜上のAlGaAsナノ構造のMOVPE選択成長」, 第47回応用物理学会北海道支部/第8回日本光学会北海道地区合同学術講演会, 札幌, 2012年1月.

4. Presentations related to other work

International conference

- [1] K. Kabamoto, R. Kodaira, S. Sakita and S. Hara: Backscattered Electron and Magnetic Force Microscopy Analyses of MnAs/InAs Heterojunction Nanowires", 28th International Microprocesses and Nanotechnology Conference (MNC 2015), Toyama, Japan, November 10-13, 2015, 12C-6-5
- [2] R. Kodaira, K. Kabamoto, S. Sakita and S. Hara: " Structural and Magnetic Characterizations of Vertical Ferromagnetic MnAs/Semiconducting InAs Heterojunction Nanowires", the 2015 International Conference on Solid State Devices and Materials (SSDM 2015), September 27-30, Sapporo, Japan, D-6-3
- [3] R. Kodaira, H. Fujimagari, H. Kato, S. Sakita and S. Hara: "Selective-Area Metal-Organic Vapor Phase Epitaxy of HeteroJunction Nanowires between Ferromagnetic MnAs and Semiconducting InAs", 27th International Microprocesses and Nanotechnology Conference (MNC 2014), Fukuoka, Japan , November 4-7, 2014, 6B-6-3
- [4] H. Kato, S. Sakita, and S. Hara: "Magnetic Characterization of Lateral MnAs Nanowires Selectively Grown by Metal-Organic Vapor Phase Epitaxy", the 17th International Conference on Metal-Organic Vapor Phase Epitaxy (ICMOVPE-XVII), Lausanne, Switzerland, July 13-18, 2014.
- [5] M. Fischer, M. T. Elm, S. Sakita, S. Hara, and P. J. Klar: "Transport Measurements on Individual Ferromagnetic MnAs Nanocluster Arrangements", the 2014 German Physical Society (DPG) Spring Meeting (Dresden 2014), Dresden, Germany, March 30-April 4, 2014, MA23.9.
- [6] M. Fischer, S. Sakita, H. Kato, M. T. Elm, S. Hara, and P. J. Klar: "Magnetotransport Measurements on Individual MnAs Nanoclusters and Nanocluster Arrangements", the 2013 Material Research Society (MRS) Fall Meeting, Boston, Massachusetts, USA, December 1-6, 2013, U5.05.
- [7] H. Kato, S. Sakita, M. Fischer, and S. Hara: "Fabrication and Characterization of Lateral MnAs Nanowires by Selective-Area Metal-Organic Vapor Phase Epitaxy", the 26th International Microprocesses and Nanotechnology Conference (MNC 2013), Sapporo, Japan, November 5-8, 2013, 7D-4-2.
- [8] H. Fujimagari, S. Sakita, and S. Hara: "Fabrication and Structural Characterization of Vertical Free-Standing InAs Nanowires Hybridized with Ferromagnetic MnAs

- Nanoclusters”, the 2013 International Conference on Solid State Devices and Materials (SSDM 2013), Fukuoka, Japan, September 24-27, 2013, PS-13-6.
- [9] S. Hara, H. Fujimagari, S. Sakita, and M. Yatago: “Difference in Formation of Ferromagnetic MnAs Nanoclusters on III-V Semiconducting Nanowire Templates”, the Nano Science + Engineering Conferences, the SPIE Optics + Photonics Conferences 2013, San Diego, California, USA, August 25-29, 2013, 8820-30.
- [10] M. Fischer, S. Sakita, M. T. Elm, P. J. Klar, and S. Hara: “Selective-Area Growth of MnAs Nanoclusters for New Planar Magnetoelectronic Devices”, the 4th International Symposium on Organic and Inorganic Electronic Materials and Related Nanotechnologies (EM-NANO 2013), Kanazawa, Japan, June 17-20, 2013, P1-55, p. 101.
- [11] Y. Kohashi, S. Sakita, S. Hara, and J. Motohisa: “Selective-Area Growth of Highly Uniform and Thin InGaAs Nanowires by Two-Step growth Method”, the 2012 Material Research Society (MRS) Fall Meeting, Boston, Massachusetts, USA, November 25-30, 2012, FF9.01.
- [12] Y. Kohashi, S. Sakita, S. Hara, and J. Motohisa: “Control of Diameter and Pitch of InGaAs Nanowire Arrays in Selective-Area Metal-Organic Vapor-Phase Epitaxy”, the 2012 International Conference on Solid State Devices and Materials (SSDM 2012), Kyoto, Japan, September 25-27, 2012, C-2-3.

Domestic conference

- [1] 小平 竜太郎, 梶本 恭平, 崎田 晋哉, 原 真二郎: 「MnAs/InAsダブルヘテロ接合ナノワイヤの作製と評価」, 第 76 回応用物理学会秋季学術講演会, 名古屋, 2015 年 9 月
- [2] 小平 竜太郎, 藤曲 央武, 加藤 弘晃, 崎田 晋哉, 原 真二郎: 「MnAs/InAsナノワイヤの作製と成長条件依存性評価」 第 75 回応用物理学会秋季学術講演会, 札幌, 2014 年 9 月
- [3] 加藤 弘晃, 崎田 晋哉, 原 真二郎: 「SA-MOVPE法により作製した横型MnAsナノワイヤの評価」, 第 49 回応用物理学会北海道支部/第 10 回日本光学会北海道地区合同学術講演会, 札幌, 2013 年 12 月.
- [4] 藤曲 央武, 崎田 晋哉, 原 真二郎: 「III-V族化合物半導体ナノワイヤ上の強磁性体MnAsナノクラスタ複合構造の作製と構造評価」, 第 74 回応用物理学会秋季学術講演会, 京都, 2013 年 9 月
- [5] 加藤 弘晃, 崎田 晋哉, Martin Fischer, 原 真二郎: 「MOVPE選択成長法による横型MnAsナノワイヤの作製と評価」, 第 74 回応用物理学会秋季学術講演会, 京都, 2013 年 9 月.
- [6] 藤曲 央武, 崎田 晋哉, 原 真二郎: 「InAsナノワイヤ上の強磁性体MnAsナノクラスタ複合構造の作製と評価」, 第 60 回応用物理学会春季学術講演会, 厚木, 2013 年 3 月.

- [7] 藤曲 央武, 崎田 晋哉, 原 真二郎: 「MnAsナノクラスタ及びInAsナノワイヤによるヘテロ構造の選択成長と構造評価」, 第 48 回応用物理学会北海道支部/第 9 回日本光学会北海道地区合同学術講演会, 釧路, 2013 年 1 月.
- [8] 小橋 義典, 崎田 晋哉, 原 真二郎, 本久 順一: 「2 段階MOVPE選択成長による極微細・位置制御InGaAsナノワイヤの形成」, 第 73 回応用物理学会学術講演会, 松山, 2012 年 9 月.
- [9] 矢田郷 昌稔, Matthias Thomas Elm, 崎田 晋哉, 原 真二郎: 「強磁性体MnAsナノクラスタ及びGaAsナノワイヤによる複合構造の選択成長」, 第 47 回応用物理学会北海道支部/第 8 回日本光学会北海道地区合同学術講演会, 札幌, 2012 年 1 月.